Synthesis of Zinc Chalcogenide Nanocrystals as Hosts for Optically Active Defects

Ratul Mangal

A thesis

submitted in partial fulfilment of the

requirements for the degree of
Master of Science

University of Washington

2026

Committee:
Dr. Brandi M. Cossairt

Dr. Dianne Xiao

Program authorized to offer degree:
Department of Chemistry

University of Washington

Abstract

Synthesis of Zinc Chalcogenide Nanocrystals as Hosts for Optically Active Defects

Ratul Mangal

Chair of the Supervisory Committee:

Dr. Brandi M. Cossairt

Department of Chemistry

Doped zinc chalcogenide nanocrystals represent a promising materials platform for quantum information science, offering wide bandgaps, low nuclear spin environments, and the potential to host optically addressable defect states such as neutral shallow donors and lanthanide 4f emitters. This thesis describes the synthesis and characterization of doped ZnO and ZnS nanocrystals as candidate hosts for such states, pursued through three synthetic thrusts of increasing complexity. The first thrust targeted In^{3+}-doped ZnO nanorods through alkaline hydrolysis of zinc acetate in ethanol. Despite systematic variation of temperature, precursor concentration, base identity, and addition rate, the synthesis consistently produced oblate wurtzite ZnO nanocrystals rather than the desired anisotropic morphology, attributed to the absence of selective facet-capping agents in the reaction system. The second thrust employed pre-formed $Ti_8Yb_2O_{12}(PhCOO)_{16}$ heterometallic clusters as seeds for ZnO shell growth, targeting the Yb^{3+} $^2F_{5/2} \rightarrow {}^2F_{7/2}$ transition at ~980 nm. Synthesis in both dimethylacetamide and dimethyl sulfoxide produced ZnO-containing products confirmed by XRD and near-band-edge photoluminescence, but no Yb^{3+} emission at 980 nm was observed, indicating unsuccessful energy transfer from the ZnO host to the dopant. DMSO was found to reduce trap emission relative to DMA, attributed to its stronger coordinating character.

The third thrust pursued In^{3+}-doped ZnS nanorods by solvothermal synthesis using ethylenediamine as a structure-directing agent. Water-based synthesis successfully produced wurtzite ZnS with ICP-OES-confirmed indium incorporation across concentrations of 0.05–10 mol%, and systematic bandgap narrowing with increasing dopant concentration was observed. All samples were dominated by broad defect-mediated emission attributed to surface hydroxylation from aqueous synthesis conditions. A subsequent anhydrous, air-free synthesis using dry DMF as co-solvent yielded a product with dramatically improved optical properties, exhibiting a sharp emission at 377 nm with FWHM of 101–103 meV. Unexpectedly, XRD characterization identified the product as the ZnS·ethylenediamine

hybrid phase (ZnS·en) rather than wurtzite ZnS. HRTEM imaging revealed a hierarchical assembly mechanism in which ~2 nm ZnS·en nuclei bridge laterally into larger plate-like structures via bidentate ethylenediamine linkers. A systematic amine functionality study comparing no amine, monoamine (oleylamine), and diamine (ethylenediamine) provided direct experimental evidence that bidentate coordination geometry, not amine functionality alone, is the necessary condition for hybrid phase formation. Oleylamine-passivated samples exhibited improved emission intensity relative to the amine-free control without any change in crystal structure, consistent with surface passivation of zinc dangling bonds. Solvothermal treatment of the ZnS·en hybrid in DMF at 200°C produced a product consistent with wurtzite ZnS by XRD, demonstrating a viable two-step solution-phase conversion route. Together, these results establish the synthetic conditions governing phase selectivity and optical quality in ethylenediamine-directed ZnS synthesis, and identify anhydrous hybrid-to-wurtzite conversion as a promising avenue for producing phase-pure wurtzite ZnS nanocrystals suitable for future quantum optical characterization.

Table of Contents

1. Introduction

1.1 Motivation

Doping of bulk semiconductor materials is a well-established practice that is fundamental to controlling the properties of these materials. More recently, efforts have been focused on doping these materials at the nanoscale. The applications of these materials are wide-ranging, owing to the various degrees of freedom available in their synthesis. These include the identity of the host material, the size and morphology of the host crystal, the identity of the dopant species, the concentration of said species, and the depth of the dopant's incorporation into the crystal structure. By modulating these structural attributes, the magnetic, optical, and electronic properties of the resultant material may be precisely controlled.

Doped magnetic nanoparticles (DMNPs) of various forms have been used in biomedicine, biosensing, environmental remediation, energy conversion, and energy storage.[1] Gd^{3+}-doped cobalt ferrite was used in a controlled-release drug delivery mechanism for the anticancer drug curcumin.[2] Sr^{2+} and Gd^{3+}-doped Fe_3O_4, Mn-doped Fe_3O_4 showed promise in inducing magnetic hyperthermia to treat cancer.[3][4] Ni and Co-doped Fe_3O_4 was used to demonstrate concentration-dependent hemolysis.[1] Cu-doped Fe_3O_4 was additionally demonstrated as a potential alternative to formaldehyde in neutralizing bacterial toxins.[5] Magnetic filtration using Zn-doped $CoFe_2O_4$ and $MnFe_2O_4$ was used to demonstrate cleaning or recovery of oil, cadmium, methylene blue, and poly (ethylene terephthalate) pollutants from water.[6-9] Cu-doped Fe_3O_4 was also used to demonstrate degradation of organic pollutants via H_2O_2 activation.[10] Co-doped $ZnFe_2O_4$ demonstrated enhancement of specific capacitance, which may be of use in energy storage devices.[11][12] The fundamental properties of nanoscale dilute magnetic semiconductors (DMSs) have also been harnessed for spintronics, such as their "giant" Zeeman splitting, which has been used to create spin-polarized currents.[13] Additionally, Co-doped Fe_3O_4 showed switchable induction heating properties, which may be useful for advanced spintronic devices.[14]

Luminescent dopants are also of great interest. They are valued because of their tunability, precision, and bright, stable emission. The use of dopants allows access to a greater range of frequencies than with only the host crystal. It can also help to focus the material's emission by becoming the primary radiative relaxation pathway. This also has the result of broadening the useful excitation spectrum. Interest in doped semiconductor luminescence began in 1994, when a synthesis of Mn-doped ZnS was published.[15] Since then, hundreds of such materials have been developed and improved. Presently, Mn, Cu, and Ag are the most well-studied dopants.[16] Some prominent examples are Cu-doped ZnS, ZnSe, CdS, and InP, with respective blue-green, yellow-green, orange-red, and near IR emission maxima.[17-20] Cu was also doped into ternary Zn-In-S nanocrystals, yielding bright green emission with photoluminescence quantum yield (PLQY) above 80%.[21] Ag has been doped into CdZnS, CdSe, and PbSe nanocrystals, which show PLQY increasing in conjunction with dopant concentration.[22-24] Several doped nanoparticles are now commercially available, most commonly Mn- and Cu-doped ZnSe quantum dots with tunable emission and quantum yields above 50%;[25][26] Al:ZnO nanoparticles are also sold.[64] A key challenge in this area remains the ability to precisely control the number and position of dopants in each individual nanocrystal of an ensemble, especially in colloidal syntheses.

Figure 1: *Commercially available Mn-doped ZnSe (left) and Cu-doped ZnS (right). Images courtesy of NN-labs and PhysicsOpenLab.*[25][65]

Such dopants have also raised interest for potential applications in quantum information science. A major challenge in the successful creation of commercial quantum computers has been the scalability of current qubit systems. A colloidal synthesis of viable qubits would mitigate this problem greatly. There are several types of qubit systems, of which doped nanocrystals fall into the defects in solids category. In general, such a host material should have a suitable bound state, a polarizing optical pumping cycle, spin-conserving luminescence that differs from the pumping frequency, optical transitions that do not interfere with the host material, and bound states that are far apart in energy.[27] To fulfill these requirements, a host material typically needs a wide bandgap, small spin-orbit coupling, constituent elements with no nuclear spin, and needs to be available at high quality and purity.[28] ZnO is a promising material in this regard. It has a wide, direct bandgap, 4s orbitals with L=0, is isotopically purifiable, and has been shown to host neutral shallow donors that can act as a suitable bound state. These donor states have been created with Al, Ga, and In doping.[29] ZnS shares many of these properties, though it has not yet been shown to create neutral donor states as in ZnO. Thus, both have garnered interest for use as potential qubit hosts.

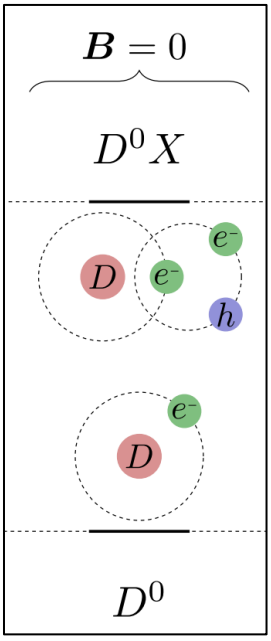

Figure 2: *Energy level diagram of the neutral shallow donor system in ZnO at zero magnetic field. The upper state D^0X represents the donor-bound exciton, in which a neutral donor captures a free exciton to form a complex of two electrons and one hole. Radiative recombination of this complex produces a sharp emission line as the system returns to the neutral donor ground state D^0. Adapted from Viitaniemi et al., Nano Letters, 2022, 22, 2134–2139. Copyright 2022 American Chemical Society.*[30]

While it has many advantages, doping can also exacerbate existing phenomena that may impact the usefulness of the material by reducing, for example, luminescence quantum yield. One such loss pathway is Auger recombination, wherein an exciton will transfer its energy to another charge carrier, rather than emitting it as a photon. This secondary carrier will release the energy through collision with the host lattice and return to the ground state, effectively resulting in non-radiative relaxation of the primary carrier. Because the probability of Auger recombination is dependent on the ability of carriers to interact, it increases with the concentration of carriers.[32] Dopant atoms introduce additional intermediate states within the bandgap, ergo a higher carrier concentration that often increases Auger recombination. Another loss pathway is through surface trapping. The presence of unpassivated “dangling” bonds on the nanocrystal surface, as well as interstitial and vacancy defects, creates

localized energy levels within the bandgap where the carrier exciton can become “trapped.” The resulting trap states often have long lifetimes due to reduced wavefunction overlap and the high thermal energy required for the exciton to re-enter the valence or conduction bands. The inclusion of dopant elements, especially at higher concentrations, may disrupt the crystal structure of the host material and increase the incidence of such defects. In addition, doping can affect morphological control in colloidal syntheses.[33] In indium-doped ZnO, Wang et al. (Fig 3.) showed a change in crystal structure from cubic to hexagonal as the percentage of indium was increased from 0 to 5%.[33] Silva et al. showed that substitutional incorporation of In into ZnO produced spherical nanocrystals while pure ZnO was heart-shaped. Al and Ga substitution in the same study produced nanoflowers.[34] Gaspera et al. showed similar results; in this case Al doping produced nanopyramids, while Ga-doped, In-doped, and pure ZnO created spheres. Notably, pure ZnO also underwent oriented attachment to produce elongated shapes, while the doped nanocrystals did not.[35]

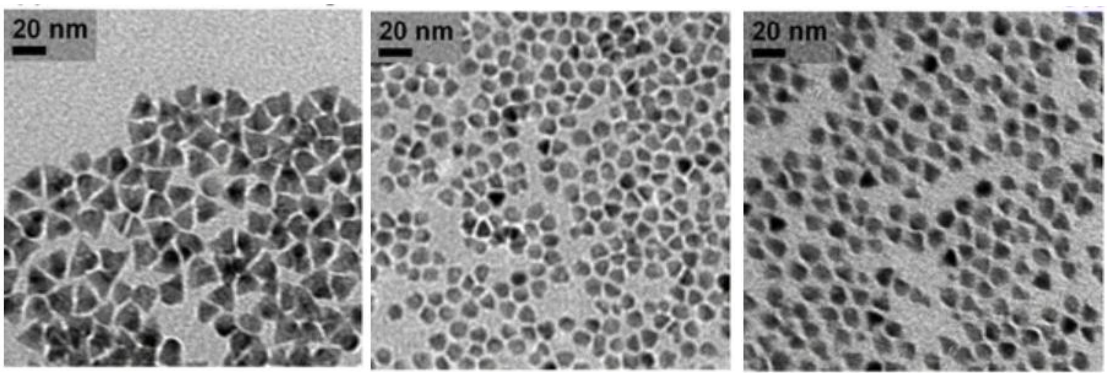

Figure 3: *Transmission electron micrographs of undoped ZnO, 2% In-doped ZnO. and 5% In-doped ZnO nanocrystals. Adapted from Wang et al. Nanoscale Res. Lett.* ***2010****, 5, 882. Copyright 2010 Springer Nature.[33]*

These challenges underscore the need for host materials that enable precise control over dopant incorporation while maintaining structural integrity and minimizing defect-mediated recombination pathways. Zinc chalcogenides represent a well-suited class of materials in this regard, offering a balance of chemical stability, tunable electronic structure, and synthetic versatility.

Zinc chalcogenides are a well-established and highly versatile class of host material. These include Zinc Oxide (ZnO), Zinc Sulfide (ZnS), Zinc Selenide (ZnSe), and Zinc Telluride (ZnTe). This thesis will focus on the former two, as the natural isotopes of their anions have a higher nuclear spin purity.[36][37] ZnO and ZnS are particularly well-known materials, with historical uses ranging from paint pigmentation and skin protection to medical imaging and incorporation in solar cells.[38-46] Within this century, these materials have also garnered significant attention for their applicability in optoelectronic devices, particularly when fabricated at the nanoscale. Large direct band gaps, the ready availability of high-quality bulk crystals, the non-toxicity of the constituent elements, and the relatively inert nature of the crystal hosts make them prime candidates for these purposes. As the behavior of dopants is strongly dictated by the intrinsic properties of the host crystals, it is worth exploring these in detail before undertaking any synthetic effort.

1.2 Properties of Zinc Chalcogenides

The crystal structures of both materials can take the zincblende or wurtzite forms. Zinc oxide may exist in both hexagonal wurtzite and cubic zincblende phases, of which wurtzite is the more common and the thermodynamically stable phase.[47] The electronic band gap of both is similar, with zincblende having a band gap of 3.44eV and the wurtzite phase having a band gap of 3.37eV.[31][48] Zinc sulfide, like zinc oxide, exists in both wurtzite and zincblende phases. Here, the zincblende structure is more thermodynamically stable at large sizes, while the wurtzite phase is more stable at the nanoscale. The band gap of these phases is larger than in ZnO, as sulfur’s valence orbitals

are higher in energy, which results in a lower VBM than oxygen.[49] The ZnS zincblende structure has a bandgap of approximately 3.66eV, while the ZnS wurtzite structure has a bandgap of approximately 3.91eV.[50] These large band gaps have made ZnS a popular material as a shell in type 1 core-shell nanoparticles.[51]

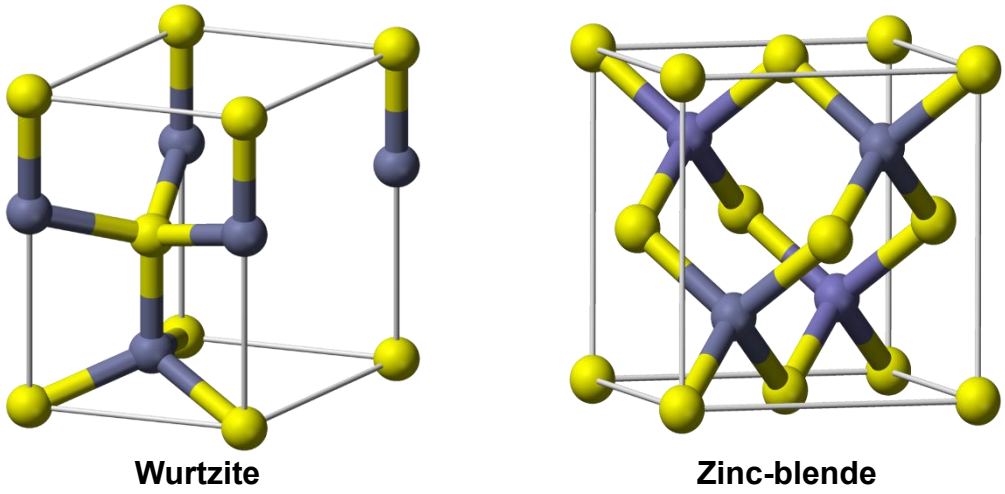

Figure 4: *Unit cell representations of wurtzite and zinc-blende crystal structures.*

Both chalcogenides are direct bandgap semiconductors, with the bandgap generally trending downwards from ZnO → ZnTe; ZnS is an exception and has the widest bandgap.[52] In general, this trend occurs because of the decreasing electronegativity and increasing anion size moving down the group. The CBM for both arises from the 4s orbitals of the Zn ion. The VBMs arise from the outermost p orbitals of the anion. The VBMs are also pushed up by the repulsion of anion p orbitals by the d orbitals of the Zn ion. This is especially pronounced in ZnO, where the Zn 3d orbitals lie just below the O 2p orbitals in energy.[53][54]

The Bohr radius, which is the distance between the electron and hole in an exciton, is the key determinant of the strength of quantum confinement and strongly influences the sensitivity of materials to dopants and defects. The exciton Bohr radius is defined by $a = \varepsilon_r \left(\frac{m}{\mu}\right) a_0$, where a_0 is the Bohr radius of a hydrogen atom (~0.053nm), m is the free electron rest mass, and μ is the reduced mass of the electron-hole pair.[55] Typical Bohr radius values for the zinc chalcogenides are given as 2.34nm for ZnO and 2.5nm for ZnS.[56][57] The increase down the group is primarily due to the materials' increasing dielectric constants. Nanocrystals synthesized in the quantum confinement regime will exhibit size-dependent perturbations to dopant energy levels and enhanced sensitivity to surface defects, both of which have direct consequences for the coherence properties of donor-bound exciton states targeted in this work.

1.3 Dopant Chemistry and Classifications

The zinc chalcogenides have been widely explored as dopant hosts. ZnO in particular has been studied as a host for at least 24 elements, including Al, Ga, In, Co, Mn, Fe, Cr, Ni, Cu, Nd, Gd, Er, Yb, N, C, S, F, Li, Mg, Ca, Ag, Au, Cd, and Sb. The remaining chalcogenides have primarily been doped with luminescent substituents, with Mn, Cu, and Co being most common. Several common dopant classifications have been summarised below in Tables No. 1-3:[15][58-63][66-68]

Table 1: Aliovalent (p/n-type) Dopants

Host Material	n-type Dopants	p-type Dopants
ZnO	Al^{3+}, Ga^{3+}, In^{3+}, F^{-}, Sb^{5+}, Cd^{2+}	N^{3-}, Li^{+}, Cu^{+}, Ag^{+}, Mg^{2+}, Ca^{2+}
ZnS	In^{3+}	Cu^{+}, Ni^{2+}

Table 2: Optically Active Dopants

Host Material	Dopant	Emission	Colour/Region
ZnO	Er^{3+}	~1540 nm	Telecom IR
ZnO	Yb^{3+}	~1000 nm	NIR
ZnO	Nd^{3+}	multi-band	IR
ZnO	Mn^{2+}	~580 nm	Yellow-green
ZnO	Co^{2+}	broad	NIR
ZnO	Cu^{2+}	broad	Visible
ZnO	Gd^{3+}	UV	UV
ZnS	Mn^{2+}	~585 nm	Yellow-Orange
ZnS	Cu^{+}	~450 nm	Blue-Green
ZnS	Eu^{2+}	~460 nm	Blue
ZnS	Dy^{3+}	~575 nm	Yellow

Table 3: Dopants of Quantum Interest

Host Material	Dopant	Mechanism
ZnO	In	Localized surface plasmon resonance (LSPR), Neutral shallow donor
ZnO	Ga	LSPR, Neutral shallow donor
ZnO	Al	LSPR, Neutral shallow donor
ZnO	Er	4f emission
ZnO	Yb	4f emission
ZnO	Mn	Spin-1/2, DMS

ZnS	Mn	Spin-1/2, single dopant
ZnS	Eu	4f emission
ZnS	Cu	Dopant emission

There are several different mechanisms of dopant incorporation that can occur in a colloidal system, and two different sites that a dopant atom can incorporate. These are represented by substitutional and interstitial dopants. Substitutional dopants occupy the place of an atom from the host lattice; for example, if In^{3+} were to replace Zn^{2+} in ZnO. This is desirable for most dopants because it is geometrically well-defined, produces predictable electronic or optical perturbations, and integrates the dopant into the host crystal lattice. The favourability of substitution is primarily governed by ionic radius mismatch, charge compensation, and crystal field compatibility. Ions that are too different in size from the host ion will cause more lattice strain and will be less favorably incorporated. Charge imbalance introduced by the dopant will also need to be compensated, often by a free electron or a compensating defect, such as a zinc vacancy. Interstitial dopants take up a space between the lattice sites of the crystal host.[69] These are generally unfavorable since they can create varying local environments and may be unstable.[70-73]

1.4 Synthetic Strategies

Colloidal synthesis has emerged as the most versatile and widely adopted approach for producing doped ZnO and ZnS nanocrystals, offering precise control over particle size, morphology, and surface chemistry. In doped ZnO systems, co-precipitation from aqueous or non-aqueous solutions remains the most common route. Mn^{2+} was incorporated into ZnO nanocrystals via forced hydrolysis of mixed zinc and dopant acetate precursors in dimethylsulfoxide, producing materials with optical and magnetic properties consistent with substitutional incorporation at Zn^{2+} sites. The dopant incorporation efficiency was strongly dependent on the relative hydrolysis rates of the host and dopant precursors, where a mismatch in reactivity leads to dopant exclusion or surface segregation rather than true lattice incorporation. Careful selection of precursors is therefore an important part of colloidal synthesis.[13][73][74]

The self-purification effect presents a particular challenge in colloidal ZnO nanocrystal synthesis. Because ZnO nanocrystals relevant to quantum confinement are typically below 5 nm in diameter, the thermodynamic penalty for substitutional dopant incorporation is significantly elevated relative to bulk. This manifests experimentally as low doping efficiencies, broad distributions of dopant environments, and a tendency for dopants to segregate to surface or near-surface sites.[75] Strategies to overcome this include the use of growth-doping protocols, where dopant precursors are introduced after initial nucleation so that they are adsorbed onto the nanocrystal surface and subsequently overgrown, and the use of organometallic precursors in high-boiling coordinating solvents that slow growth kinetics and allow thermodynamic equilibration at the crystal surface.[75] The Gamelin group has been particularly influential in establishing these design principles for transition-metal-doped ZnO, showing that dopants such as Co^{2+} and Mn^{2+} can be incorporated with high site-selectivity under appropriately controlled conditions.[60][73]

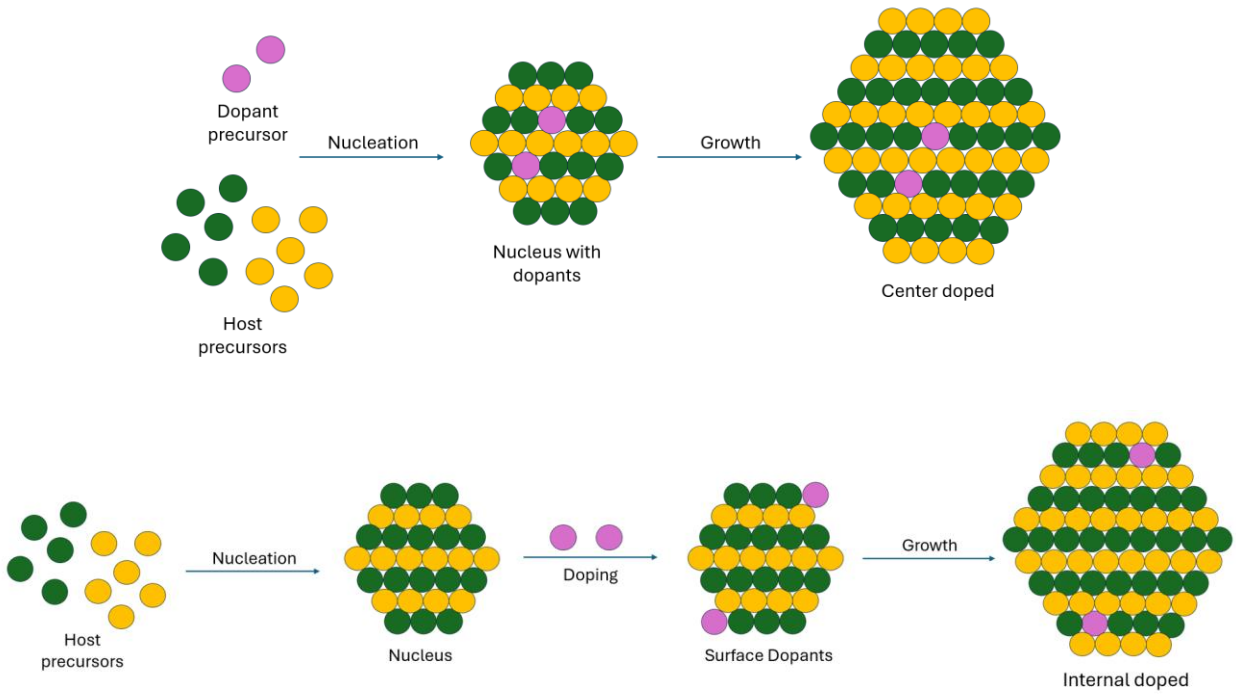

Figure 5: *Schematic of nucleation doping (top) - dopant is added at nucleation stage of crystal formation, resulting in dopants incorporated at the crystal core. Schematic of growth doping (bottom) – dopant is added after initial nucleation stage, leading to a dopant distribution dependent on when dopant was added.*

In doped ZnS nanocrystals, Mn^{2+} has served as the canonical model dopant since the early work of Bhargava et al. in the 1990s, who reported strongly enhanced Mn^{2+} luminescence in ZnS:Mn nanocrystals relative to the bulk and attributed this to quantum confinement effects on the energy transfer from the ZnS host to the Mn^{2+} $^4T_1$ excited state.[15] Counio et al. and later Norberg et al. demonstrated that the luminescence enhancement is strongly dependent on whether Mn^{2+} was substitutional or surface-bound, with surface-associated Mn^{2+} producing broadened, red-shifted emission and faster non-radiative decay.[73][76][77] This established a benchmark for the field; optical spectroscopy alone is insufficient to confirm substitutional incorporation, and characterization such as EPR is required to distinguish interior from surface dopant populations. For ZnS:Cu, colloidal co-precipitation in aqueous solution using zinc and copper acetate precursors with sulfide sources such as Na_2S or thiourea has been widely used, with Cu^+ incorporation producing a characteristic blue-green donor-acceptor pair emission that was used in early electroluminescent display applications.[78][79]

More recent colloidal strategies have moved toward non-aqueous, high-temperature synthesis in coordinating solvents to produce doped ZnO and ZnS nanocrystals with narrower size distributions and better-defined dopant environments.[80] The use of organic ligands like oleylamine, trioctylphosphine oxide (TOPO), and oleic acid as coordinating agents allows precise tuning of nanocrystal growth kinetics and surface passivation, both of which influence dopant incorporation.[81] For lanthanide-doped ZnS in particular, where the large ionic radius mismatch between Ln^{3+} and Zn^{2+} makes substitutional incorporation thermodynamically unfavorable, high-temperature non-aqueous synthesis has been shown to improve incorporation efficiency by providing sufficient thermal energy to overcome the kinetic barriers to lattice substitution while maintaining nanocrystal size control.[82][83] These advances are directly relevant to quantum information applications, where spectral homogeneity, long excited-state lifetimes, and well-defined spin environments depend on the quality and consistency of dopant incorporation achieved during synthesis.

Additionally, solvothermal synthesis is an important colloidal route for doped ZnO and ZnS nanocrystals. The method involves heating precursor solutions in sealed autoclaves above the boiling point of the solvent, generating elevated pressures that modify solubility, supersaturation, and crystal growth kinetics relative to ambient co-precipitation. For doped ZnO, hydrothermal conditions have been shown to favor anisotropic growth along the c-axis of the wurtzite structure, producing nanorods, nanowires, and hierarchical morphologies with aspect ratios tunable through pH, temperature, and the nature of capping agents present in solution. Dopant incorporation under hydrothermal conditions is governed by the same principles as in co-precipitation, but the elevated temperature and pressure environment can improve substitutional incorporation efficiency by providing greater thermal energy for lattice reorganization.[84][85] The relatively high ionic strength of solvothermal synthesis can complicate surface passivation, often producing nanocrystals with higher surface defect densities than those achieved by non-aqueous organometallic routes, which has implications for photoluminescence quantum yield and spin coherence.[86]

Diffusion doping is a fundamentally different approach to dopant incorporation. In this strategy, pre-formed undoped ZnO or ZnS nanocrystals are annealed in the presence of a dopant precursor, driving thermally activated diffusion of the dopant into the host lattice. Vlaskin et al. provided an important demonstration of this approach, showing that transition metal dopants could be introduced into pre-formed II-VI nanocrystals under thermodynamic equilibrium conditions, enabling dopant compositions and site selectivities that are difficult to achieve through kinetically controlled co-precipitation. [87] For ZnO, diffusion coefficients of common dopants such as Mn^{2+} and Co^{2+} are strongly temperature-dependent and are significantly affected by the presence of oxygen vacancies, which act as diffusion pathways through the lattice.[88]

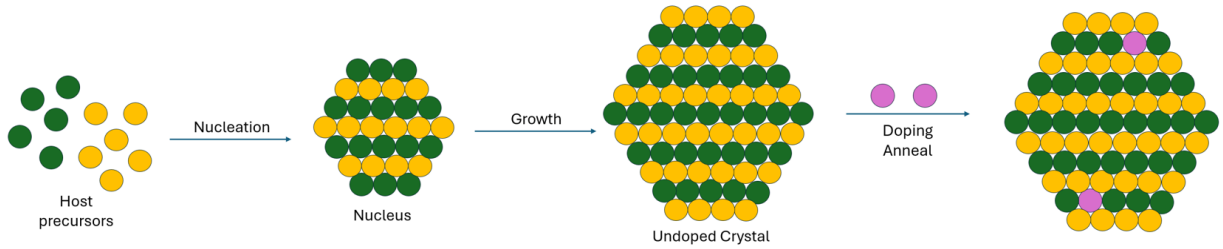

Figure 6: *Schematic of diffusion doping. Dopant is added after the crystal is fully formed and heat is applied to thermally activate diffusion of the dopant into the host lattice, resulting in a near-surface dopant distribution.*

The growth of an epitaxial shell around a doped nanocrystal core represents one of the most powerful strategies for improving the optical and spin properties of doped ZnO and ZnS nanocrystals for quantum applications. The shell serves several functions simultaneously. It passivates surface trap states, physically isolates the dopant from the nanocrystal surface and surrounding ligand environment, and can provide additional quantum confinement that modifies the energy transfer dynamics between the host exciton and the dopant.[89] In doped ZnS systems, ZnS/ZnS homostructures and ZnS/ZnSe heterostructures have been employed to improve Mn^{2+} luminescence quantum yields substantially, with the shell eliminating surface-associated Mn^{2+} populations that contribute to spectral inhomogeneity and non-radiative loss.[90][91] The choice of shell material is governed by lattice mismatch, as smaller mismatches reduce interfacial strain and the associated defect formation. Band alignment between core and shell is also an important consideration as it determines how carriers are localized in the nanocrystal.[51]

1.5 Characterization Techniques

X-ray Diffraction (XRD): XRD measures the diffraction of X-rays by crystallographic planes in a material, producing a pattern of peaks whose positions are characteristic of the crystal structure and lattice parameters. In doped nanocrystals, XRD confirms crystal structure and purity, and shifts in peak positions or width relative to the undoped host can provide evidence of successful dopant incorporation into the lattice.[33]

Transmission electron microscopy (TEM): TEM uses a focused electron beam transmitted through a thin sample to produce images of nanocrystals at atomic resolution. Scanning TEM can be combined with combined with energy-dispersive X-ray spectroscopy (STEM-EDS) to map the spatial distribution of elements across individual nanocrystals. Electron energy loss spectroscopy (EELS) provides complementary chemical information by measuring the energy lost by transmitted electrons due to inelastic scattering, enabling identification of oxidation states and bonding environments of dopant ions. This is particularly useful for investigating whether dopants are distributed throughout the nanocrystal interior or segregated to the surface.[92]

Photoluminescence (PL) spectroscopy: PL spectroscopy measures the emission of photons from a material following photoexcitation, providing information on the energy levels, radiative transitions, and defect states of doped nanocrystals, as dopant-related emission bands such as the characteristic Mn^{2+} yellow-orange emission in ZnS are directly observable.[46] Photoluminescence excitation (PLE) spectroscopy identifies which excitation wavelengths most efficiently produce a given emission, helping establish the energy transfer pathway from host to dopant. It is useful for investigating whether luminescence is emerging from the absorption source investigated.

Electron paramagnetic resonance (EPR) spectroscopy: EPR spectroscopy detects transitions between spin states of unpaired electrons in a magnetic field, making it highly sensitive to the local coordination environment of paramagnetic dopants such as Mn^{2+} and Co^{2+}. The hyperfine splitting pattern of Mn^{2+} EPR spectra is particularly diagnostic of substitutional incorporation at tetrahedral Zn^{2+} sites versus surface or secondary phase environments.[73][77]

Inductively coupled plasma optical emission spectroscopy (ICP-OES) and mass spectrometry (ICP-MS): In these techniques, a digested sample is burned in a plasma flame to ionize it. Then an emission or mass spectrum can be formed by comparing against known standards, allowing precise quantification of relative atomic percentages in a sample.

X-ray photoelectron spectroscopy (XPS): a surface-sensitive technique that probes the elemental composition and oxidation states of atoms within the top few nanometers of a nanocrystal, making it useful for distinguishing surface-bound dopants from interior populations. It does this by bombarding a solid sample with X-rays, which causes emission of photoelectrons. The kinetic energy of these matches the binding energies for specific elements that can then be identified.

1.6 Motivating the Dissertation

Thus far, we have discussed the properties of zinc chalcogenides as host materials for optically active dopants, the classification and chemistry of relevant dopants, the synthetic strategies available for their colloidal incorporation, and the characterization techniques employed to confirm dopant identity, concentration, and site selectivity. The convergence of these considerations motivates the central experimental work of this thesis: the development of colloidal synthetic routes to doped ZnO and ZnS nanocrystals capable of hosting optically active defect states for potential quantum information science applications. Specifically, the neutral shallow donor state formed by In^{3+} in ZnO, which gives rise to a sharp donor-bound exciton transition at cryogenic temperatures, and the deep 4f donor state of Yb^{3+}, with its telecom-wavelength emission near 980 nm, represent two distinct and complementary strategies for engineering optically addressable spin states within a wide-bandgap, low nuclear spin host. The transition to ZnS as an alternative host is further motivated by its comparable nuclear spin environment to ZnO, its wide bandgap, and the synthetic accessibility of its wurtzite nanorod morphology through hydrothermal methods. In section 2, we discuss the synthesis of ZnO nanocrystals, encompassing attempts to produce homogeneous In-doped ZnO nanorods through solution-phase alkaline hydrolysis and the use of $Ti_8Yb_2O_8(PhCOO)_{16}$ heterometallic clusters as seed materials for Yb-doped ZnO shell growth. In section 3, we discuss the synthesis and doping of ZnS nanorods through solvothermal methods, the characterization of their defect-mediated optical properties as a function of dopant concentration and post-synthetic annealing conditions,

and the development of an air-free, water-free synthetic protocol designed to reduce the surface defect density that presently dominates the optical response of these materials. Together, these synthetic thrusts represent a systematic effort to establish the conditions under which zinc chalcogenide nanocrystals can be produced with the structural and optical quality necessary to support future quantum optical applications.

2. General Experimental

2.1 Materials

All chemicals were used as received unless otherwise stated: Zinc acetate dihydrate (≥99%, Sigma-Aldrich), sodium hydroxide (≥97%, Sigma-Aldrich), thiourea (Spectrum Chemical), zinc nitrate hexahydrate (98%, Sigma-Aldrich), indium nitrate hydrate (99.9%, Sigma-Aldrich), potassium hydroxide (90%, Sigma-Aldrich) ethylenediamine (≥99%, Sigma-Aldrich), N-N-dimethylformamide (≥99.8%, Sigma-Aldrich), dimethylacetamide (≥99.8%, Sigma-Aldrich), dimethyl sulfoxide (≥99.9%, Sigma-Aldrich), oleylamine (70%, Sigma-Aldrich), ethanol (200 proof, Decon Laboratories), chloroform (≥99%, Lab Alley), acetone (≥99%, Lab Alley), acetonitrile (≥99.5%, Sigma-Aldrich). Dimethylformamide and ethylenediamine used in air-free syntheses were dried over CaH_2 overnight, degassed, then distilled in vacuo before being transferred into a nitrogen-filled glovebox, where they were stored over 4Å molecular sieves. Solid precursors used in air-free syntheses were dried overnight under dynamic vacuum before being transferred into a nitrogen-filled glovebox.

2.2 X-ray Diffraction (XRD)

Powder X-ray diffraction patterns were collected at the University of Washington on a Bruker D8 Discover diffractometer using Cu Kα radiation (λ = 1.5406 Å). Samples were prepared by drop casting dilute nanocrystal suspensions onto zero-background silicon wafers and allowing the solvent to evaporate prior to measurement.

2.3 Transmission Electron Microscopy (TEM)

All TEM imaging was done at the University of Washington on a FEI Tecnai G2 F20 SuperTwin microscope operated at 200 kV using bright field imaging mode. Samples were prepared drop casting 5 μL of dilute suspensions in solvent onto a suspended ultrathin carbon film on a lacey carbon support film, 400 mesh, copper grids purchased from Ted Pella Inc, and allowed to dry fully then placed under vacuum overnight. TEM size analysis was performed using manual analysis in ImageJ based off images from at least three different grid locations.

2.4 Photoluminescence Spectroscopy (PL, PLE)

Photoluminescence (PL) and photoluminescence excitation (PLE) spectra were collected at the University of Washington on an Edinburgh Instruments FLS1000 luminescence spectrometer equipped with a 450 W xenon arc lamp as the excitation source and an InP/InGaAs NIR photomultiplier tube (Hamamatsu Photonics H12397A-75) for detection. Samples were dispersed in ethanol for measurement unless otherwise stated. Air-free ZnS samples synthesized in anhydrous DMF were measured as dispersions in dry DMF without exposure to ambient atmosphere. All measurements were performed at room temperature.

2.5 X-ray Photoelectron Spectroscopy (XPS)

X-ray photoelectron spectroscopy measurements were performed at the University of Washington on a Kratos Axis Supra+ spectrometer using a monochromated Al Kα X-ray source (hν = 1486.6 eV). Survey spectra and high-resolution spectra were collected for the Zn 2p, S 2p, In 3d, C 1s, and O 1s regions. Binding energies are reported as measured without charge correction. The adventitious carbon C 1s peak observed at approximately 284.8 eV is noted as a reference, and any systematic offset from this value should be considered when interpreting absolute binding energies. Samples were prepared as dry powders drop cast on silica wafers.

2.6 Inductively Coupled Plasma Optical Emission Spectroscopy (ICP-OES)

Elemental analysis was performed at the University of Washington by inductively coupled plasma optical emission spectroscopy (ICP-OES) using a PerkinElmer Optima 8300 spectrometer. Prior to measurement, nanocrystal samples were digested by treatment with 1 mL of concentrated nitric acid and 1 mL of hydrogen peroxide, and the resulting solution was diluted to 10 mL with 18 MΩ·cm deionized water. Elemental concentrations were determined by comparison against multi-element calibration standards prepared in the same acid matrix.

2.7 UV-Vis Spectroscopy

UV-Vis absorption spectra were collected on an Agilent Cary 5000 UV-Vis-NIR spectrophotometer. Solution measurements were performed in 1 cm path length quartz cuvettes, with the neat solvent used as the reference baseline.

2.8 Diffuse Reflectance Spectroscopy (DRS)

Diffuse reflectance spectra were collected on an Agilent Cary 5000 UV-Vis-NIR spectrophotometer. Samples were drop cast onto quartz disks and the solvent allowed to evaporate. Barium sulfate ($BaSO_4$) was used as the white reference baseline. Reflectance data were converted to absorbance using the Kubelka-Munk transformation, $F(R) = (1-R)^2/2R$, where R is the measured reflectance expressed as a fraction.

3. Synthesis and Doping of ZnO Nanocrystals

3.1 ZnO Nanorod Synthesis

Indium-doped ZnO nanorods represent a particularly attractive platform for quantum information science applications due to the unique optical properties that arise from In^{3+} incorporation into the ZnO host lattice. In^{3+} substitution at Zn^{2+} sites acts as a neutral shallow donor, and at cryogenic temperatures this donor state gives rise to a sharp, narrow bound exciton emission line through the donor-bound exciton (D^0X) with optical properties highly suited to quantum optical applications. The nanorod morphology is specifically targeted here for several reasons. ZnO nanorods grow preferentially along the polar c-axis of the wurtzite structure, presenting predominantly nonpolar $\{10\bar{1}0\}$ prismatic side facets that are chemically less reactive than the polar (0001) end facets, resulting in a smaller reactive surface area. This reduced surface reactivity is expected to minimize surface trap states that could interfere with the donor-bound exciton state, including through inhomogeneous broadening from surface electric fields and enhanced non-radiative decay, both of which would be detrimental to the coherence properties required for quantum information applications. For this reason, the synthesis of homogeneous, high-quality ZnO nanorods through a colloidal route was attempted as the first synthetic thrust.

3.1.1 Experimental and Results

A solution-phase synthesis based on the alkaline hydrolysis of zinc acetate in ethanol was employed as the basis for all nanorod synthesis attempts. In an example synthesis, 1463.33 mg of zinc acetate dihydrate ($Zn(OAc)_2 \cdot 2H_2O$, 6.67 mmol) was dissolved in 6.67 mL of absolute ethanol in a three-neck round bottom flask, and 533.33 mg of sodium hydroxide (NaOH, 13.33 mmol) was dissolved separately in 13.33 mL of ethanol, giving a NaOH:Zn^{2+} molar ratio of 2:1. The NaOH solution was then added dropwise to the zinc acetate solution under continued nitrogen flow and stirring. The combined solution was ramped to 60°C over approximately 10 minutes and held at this temperature with mild stirring for 24 hours. After cooling to room temperature, the product was isolated by centrifugation, the supernatant was discarded, and the precipitate was washed sequentially with absolute ethanol and deionized water to remove residual acetate and sodium ions before drying in air.

To investigate the effect of reaction conditions on nanocrystal morphology, a series of experimental variations were tested. Reaction temperature was varied between 60°C and 120°C (pentanol was used for higher temperature reactions). Reaction time was varied from 4 hours to 48 hours to probe the temporal evolution of nanocrystal morphology. Precursor concentrations were varied by scaling the zinc acetate and NaOH quantities while maintaining the 2:1 NaOH:Zn^{2+} molar ratio, to assess the effect of supersaturation on nucleation density and subsequent growth. Syntheses were conducted in both air and an inert (nitrogenous) environment. Precursor ratios were also varied. To attempt to induce faster or slower nucleation and favor rod growth, different bases of LiOH, KOH, and NaOH were tested, as well as varying the addition rates of these reagents. Finally, oriented attachment was investigated as a potential route to anisotropic nanostructures, where nanocrystals produced during an initial spherical-particle synthesis were retained and used as seeds for a subsequent synthesis, with the intention of promoting preferential attachment along the c-axis to extend rod-like structures from pre-formed nuclei. In this last case, the temperature was raised to 75°C. Despite many efforts, the synthetic route was unable to produce nanocrystals of sufficient homogeneity, desired shape, or desired quality.

The table below summarizes a selection of experimental conditions and shows TEM images of the resulting nanocrystals. All show significant aggregation of particles, and none create the desired homogeneous nanorods.

Table 4: Summary of Selected ZnO Synthetic Attempts

Synthetic Variation	Resulting Nanocrystals	Representative TEM Image	Sizing
1M NaOH	Oblate nanocrystals of wurtzite crystal structure	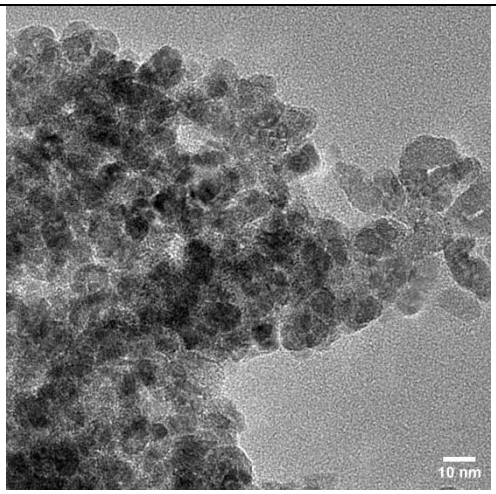	Average length: 8 ± 2nm Average width: 11 ± 2.9nm

2M KOH	Oblate nanocrystals of wurtzite crystal structure	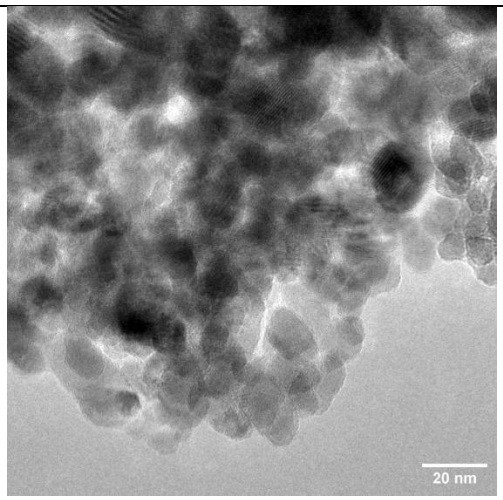	Average length: 12.5 $\pm$ 4.4nm Average width: 8.7 $\pm$ 2.3nm
5:1 OH^-:Zn^{2+}	Oblate nanocrystals of wurtzite crystal structure. Nanocrystals are most spherical of syntheses.	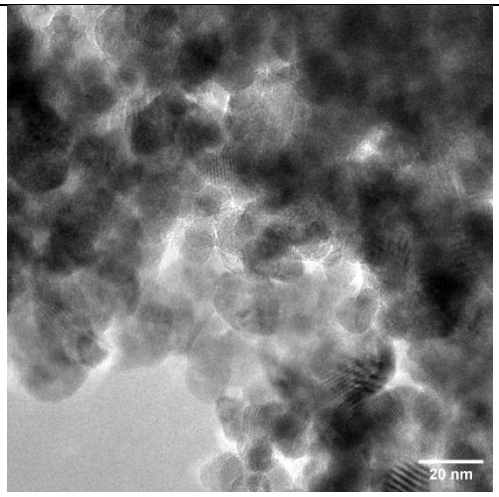	Average length: 13 $\pm$ 4.4nm Average width: 14 $\pm$ 4.9nm
2M NaOH	Oblate nanocrystals of wurtzite crystal structure. Nanocrystals are more elongated as compared to other syntheses.	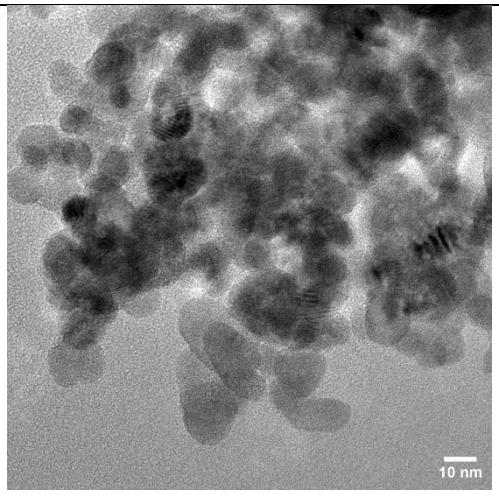	Average length: 13 $\pm$ 3.4nm Average width: 8 $\pm$ 1.8nm

Reflux of spherical ZnO nanoparticles	Oblate nanocrystals of wurtzite crystal structure. Some rod formation observed.	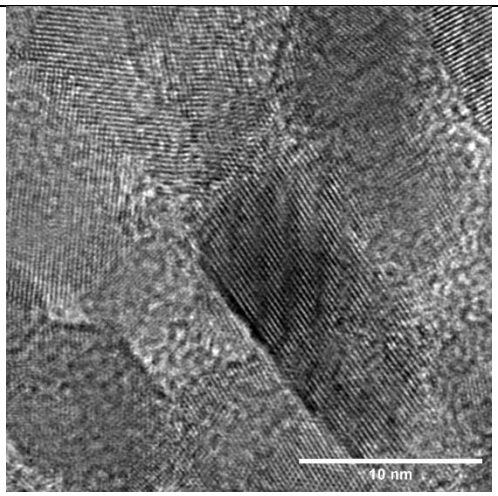	Average length: 13.9 ± 6.9nm Average width: 8.2 ± 2.6nm

Though the desired wurtzite crystal structure was achieved (as confirmed by XRD), this synthetic thrust was unable to produce the desired outcome. For this reason, it was eventually abandoned.

3.2 Seeded Growth of ZnO Using TiYb Clusters

Ytterbium-doped ZnO represents a distinct doping strategy from the shallow donor approach pursued with In^{3+}, targeting instead the deep donor states introduced by Yb^{3+} incorporation into the ZnO host lattice. The 4f electronic configuration of Yb^{3+} gives rise to a $^2F_{5/2} \rightarrow {}^2F_{7/2}$ transition at approximately 980 nm.[93] This is a wavelength of significant practical interest for quantum information applications as it falls within a low-loss optical fiber transmission window and is compatible with established telecommunication infrastructure. The shielding of the 4f orbitals by the outer $5s^25p^6$ shell renders this transition highly insensitive to the local phonon environment, producing narrow, long-lived emission with coherence properties favourable for quantum optical applications. Crucially, rather than introducing Yb^{3+} as a free ionic dopant during nanocrystal growth, the strategy pursued here attempts to use pre-formed $Ti_8Yb_2O_{12}(PhCOO)_{16}$ clusters (Fig. 7) as seeds on which to shell ZnO, with the hope of forming ZnO nanocrystals doped with paired Yb deep donors. These clusters, received from Devin Rollins in Professor Diane Xiao's group at the University of Washington, have a diameter of approximately 3 nm as determined by dynamic light scattering.

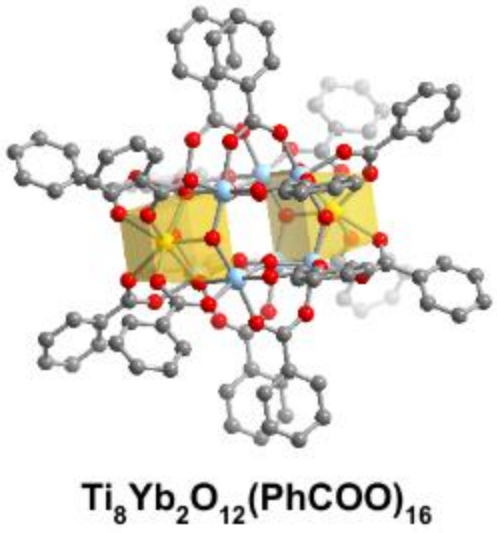

Figure 7: *Schematic of TiYb cluster used as precursor.*

3.2.1 Experimental and Results

Initial syntheses were carried out in dimethylacetamide (DMA) as solvent, chosen for its high boiling point, and good solubility for both the cluster and zinc precursors. In a typical synthesis, $Ti_8Yb_2O_{12}(PhCOO)_{16}$ clusters were dissolved by stirring in 1 mL of DMA at 80°C for 24 hours to ensure complete dissolution, giving a cluster concentration of 0.01 M. Separately, zinc acetate ($Zn(OAc)_2$) was dissolved in 4 mL of DMA at 0.05 M by stirring at 80°C for 10 minutes, and potassium hydroxide (KOH) was dissolved in 2 mL of DMA at 0.1 M by stirring for 5 minutes. All three solutions were maintained at 80°C prior to combination.

With the cluster solution still at 80°C, the zinc acetate solution was added rapidly to the cluster solution. The KOH solution was then added dropwise to the combined solution to initiate hydrolysis and condensation of the zinc precursor. The reaction mixture was maintained at 80°C for 5 hours to allow shell growth and crystallization. In cases where precipitation did not occur spontaneously, additional 0.1 M KOH in DMA was added slowly until precipitation was induced, after which the mixture was allowed to ripen for a further 1 hour before cooling to room temperature naturally. The precipitate was collected by centrifugation and washed sequentially with water and acetone to remove residual solvent and unreacted precursors. This initial attempt did result in the formation of wurtzite ZnO, as confirmed by XRD.

Further synthetic attempts focused on reducing the extraneous nucleation of ZnO to focus the reagent material towards cluster shelling. The temperature was reduced to 72°C to slow the nucleation rate. The rate of base addition was also reduced. In addition, the addition of the zinc precursor was done simultaneously with the base to mitigate localized extraneous nucleation of pure ZnO nanoparticles. Though ZnO crystals were produced, these synthetic attempts also resulted in significant trap emission as shown in PL spectra. The emission of Yb was also not able to be observed at room temperature, again indicating a lack of Yb incorporation. In similar studies on Yb doped CeO_2, a small amount of emission from the Yb dopant was observed at room temperature, and so it was expected that a high-quality shelled crystal may show the same.

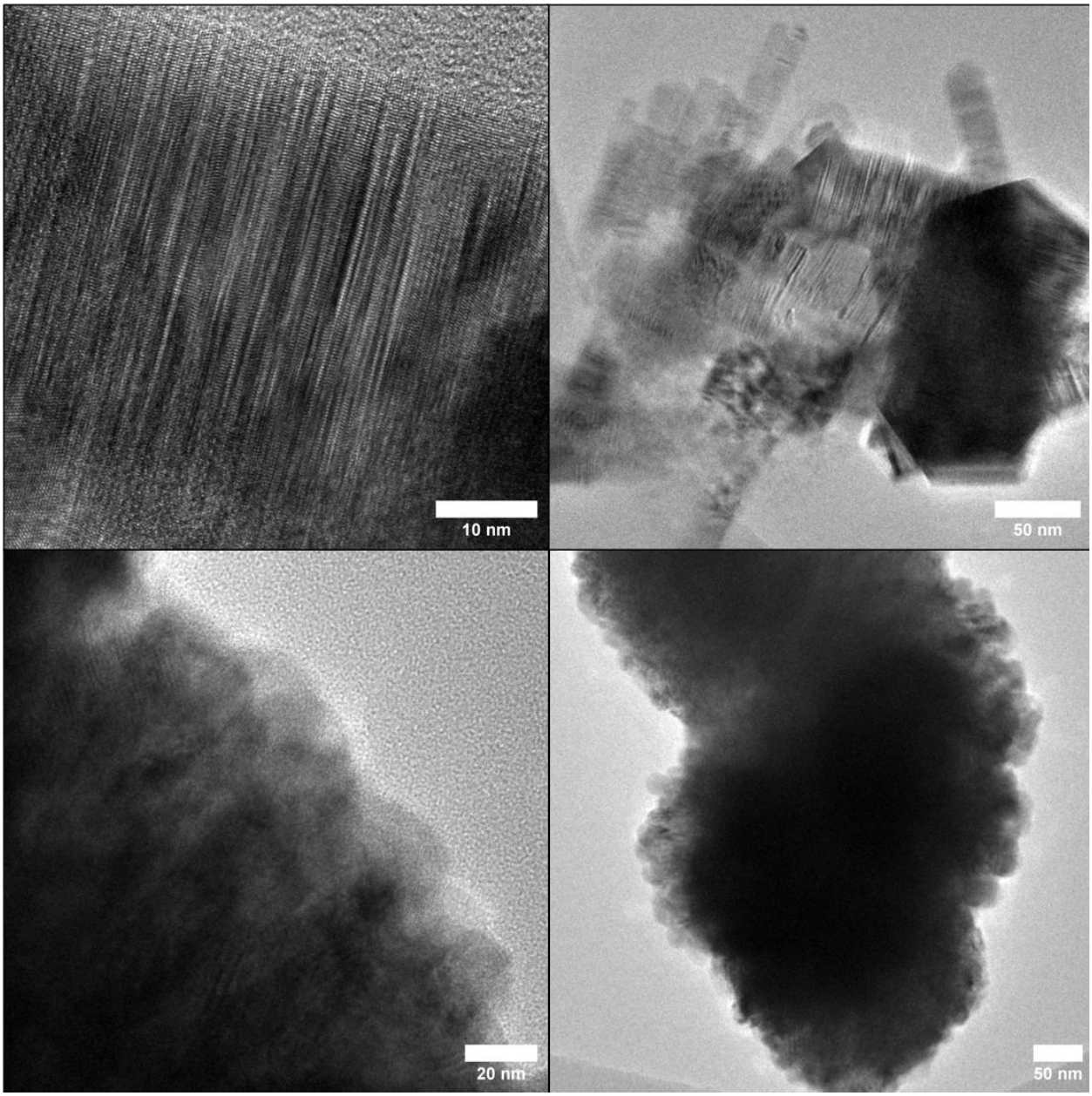

Figure 8: *TEM and HRTEM images of ZnO synthesized in DMA (top) and DMSO (bottom) solvents.*

Figure 8 shows TEM and HRTEM images of ZnO nanocrystals produced in the presence of the $Ti_8Yb_2O_{12}(PhCOO)_{16}$ cluster in DMA and DMSO solvents respectively. In both cases, the products show irregular morphologies with significant polydispersity, consistent with uncontrolled nucleation of ZnO rather than directed shell growth on the cluster surface. The DMA synthesis produced larger, rod-shaped particles of varying aspect ratios, with evidence of stacking faults visible in the HRTEM images. The DMSO synthesis produced smaller, more aggregated particles, suggesting that the stronger coordinating character of DMSO moderates the ZnO nucleation kinetics relative to DMA.[94] However, neither solvent produced the well-defined core-shell morphology that would be expected from successful heterogeneous nucleation of ZnO on the cluster surface. The absence of a distinct ~3nm core consistent with the cluster dimensions in either TEM dataset suggests that the cluster either dissolved under the synthesis conditions, was not successfully incorporated into the growing ZnO particles, or is present but

indistinguishable from the ZnO matrix at the resolution achieved. The prevalence of stacking faults in the DMA product is consistent with rapid, kinetically driven ZnO growth that does not allow sufficient time for crystallographic ordering, and may be contributing to the high trap state density observed in the optical measurements.

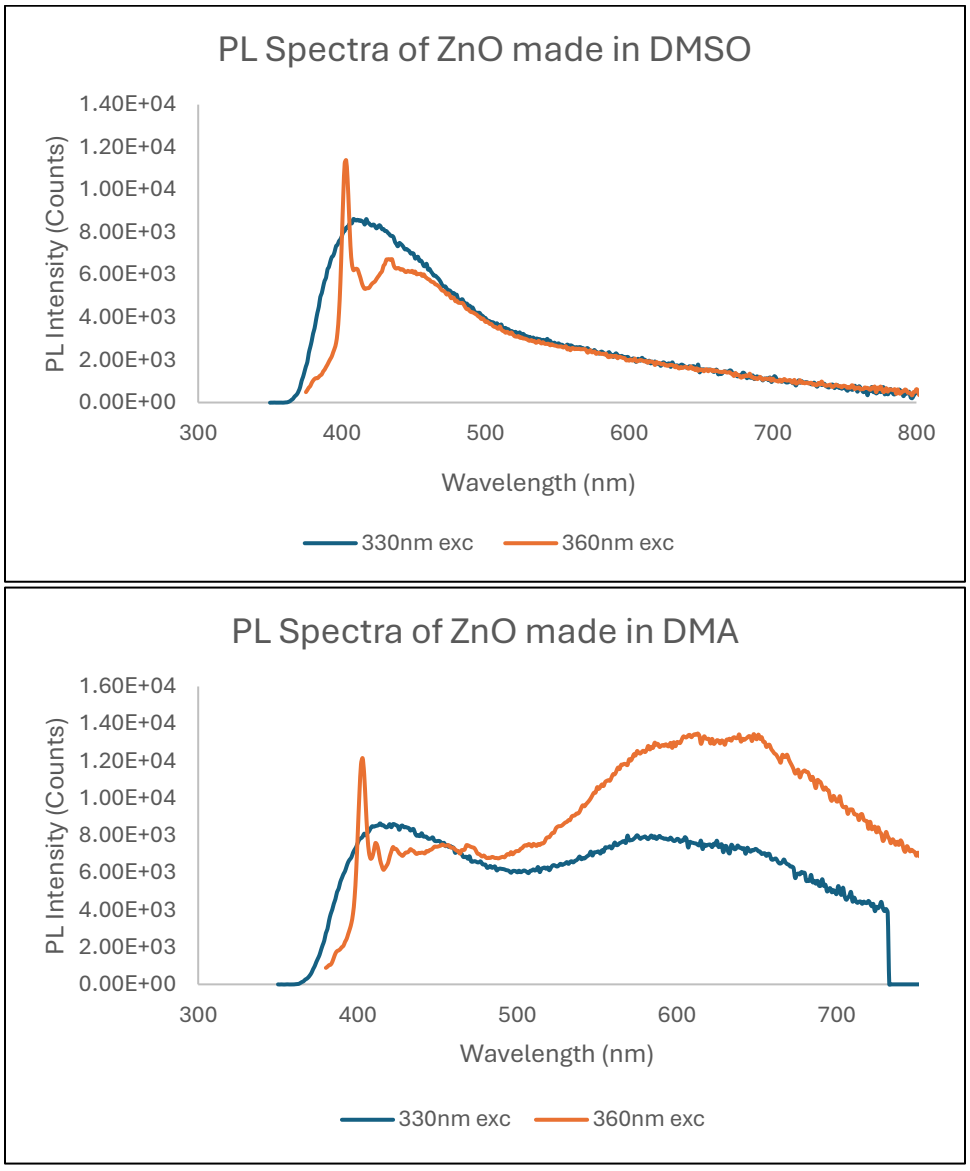

Figure 9: *PL spectra of ZnO made in both DMA and DMSO solvents, in the presence of cluster. Excitation wavelengths at 330nm and 360nm are shown.*

Figure 9 shows photoluminescence spectra of the DMA and DMSO synthesis products at excitation wavelengths of 330nm and 360nm. A sharp emission feature at ~403nm is observed under 360nm excitation but is absent under 330nm excitation. This is attributed to near-band-edge emission from ZnO, selectively excited at 360nm which lies close to the ZnO bandgap energy. However, it may equally arise from an interstitial zinc defect. The absence of this feature under 330nm excitation may be due to hot carrier thermalization at higher excitation energies, where carriers excited well above the band edge rapidly relax through phonon-mediated processes and preferentially populate sub-bandgap trap states rather than recombining radiatively at the band edge. The extraneous peaks between 400-

500nm could be from Ti species in the sample mix, or from benzoate ligands in the cluster. Both samples show broad defect emission spanning 500-800nm with no observable sharp near-band-edge emission, confirming that the ZnO produced in both cases contains a high density of sub-bandgap trap states regardless of solvent choice. The larger amount of trap emission seen in the DMA sample could be for a number of reasons. Crystals made in DMA were rod-shaped and larger than those in DMSO, leaving more surface area for surface trap states to occur. DMSO also slows nucleation, potentially resulting in better crystallinity. Lastly, DMSO may simply be a better surface passivating ligand. Critically, no emission near 980nm attributable to the Yb^{3+} $^2F_{5/2} \rightarrow {}^2F_{7/2}$ transition was observed in either sample at room temperature, indicating that Yb^{3+} was not successfully incorporated into the ZnO host in a configuration that allows energy transfer from the ZnO exciton to the dopant. This could reflect the failure of ZnO shell formation on the cluster surface, efficient non-radiative quenching of Yb^{3+} emission by surface defects, or thermal quenching of the Yb^{3+} excited state at room temperature.

4. Synthesis and Doping of ZnS Nanocrystals

4.1. Solvothermal Synthesis and Doping of ZnS Nanorods

Pursuing doped ZnO resulted in significant difficulties, with rod creation not achieved as a reasonable proportion of samples. Reproducibility of results was also difficult, possibly due to localized variation in reagent conditions driving nucleation. Therefore, a new synthetic thrust was chosen. ZnS was chosen as a new candidate host material because it has similar properties to ZnO that make it potentially suitable as a qubit host, especially a low incidence of naturally occurring isotopes with nuclear spin. The most abundant isotopes of both zinc (^{64}Zn, ^{68}Zn, ^{70}Zn) and sulfur (^{32}S, ^{34}S) carry zero nuclear spin, meaning that the dominant isotopic constituents of the ZnS lattice are nuclear-spin-free. This places ZnS alongside ZnO as a low nuclear spin host, favorable for preserving electron spin coherence of incorporated donor states. The wider bandgap of the wurtzite ZnS phase relative to zinc blende ZnS additionally offers a larger energy window within which donor-bound exciton states can be spectrally resolved from other optical transitions. It is also favorable for nanorod growth as the hexagonal crystal structure can preferentially align along the c-axis and grow into nanorods. The nanorod morphology was targeted for the same reasons discussed in the context of ZnO.

Though In-doped ZnS has not been explicitly tested as a qubit system, the viability of indium as a shallow donor dopant in ZnS can be assessed theoretically from the known electronic and optical properties of the host material. Wurtzite ZnS has an electron effective mass of $m_e \approx 0.25–0.34\ m_0$, a hole effective mass of $m_h \approx 0.6–0.8\ m_0$, and a relative permittivity of $\varepsilon_r \approx 8.1–8.9$, giving an exciton Bohr radius of approximately 2.4–2.5 nm.[95][96] The exciton binding energy calculated from these parameters is $E_B \approx 35–40$ meV, which exceeds the thermal energy at room temperature ($k_BT \approx 25$ meV), showing that excitons in ZnS are stable at room temperature. The shallow donor ionization energy can be estimated using the effective mass approximation, which gives the donor binding energy as:

$$E_D \approx \frac{m_e^*}{\varepsilon_r^2} \times 13.6\ \text{eV} \approx 20 - 40\ \text{meV}$$

This places the donor state only 20–40 meV below the conduction band minimum. This is consistent with a shallow donor that will likely be thermally ionized at room temperature but likely remains bound at cryogenic temperatures. The validity of this approximation is supported by comparison with aluminium, a known dopant in ZnS, whose effective mass is only marginally perturbed upon doping ($m^*_e = 0.24\ m_0$ for pure ZnS versus $0.22\ m_0$ for Al-doped ZnS), confirming that substitutional group III dopants do not strongly perturb the host band structure. Since In^{3+} is isoelectronic with Al^{3+} in terms of its donor character (both substitute at Zn^{2+} sites and contribute one excess electron to the conduction band), indium is expected to behave similarly as a shallow donor, making In:ZnS a theoretically well-motivated target for low-temperature donor-bound exciton spectroscopy relevant to quantum information applications.

4.1.1 Experimental

Wurtzite ZnS nanorods were synthesized using a solvothermal method adapted from the literature,[97] with ethylenediamine as a structure-directing agent to promote anisotropic growth along the c-axis. In a typical synthesis, thiourea (1.2 M) and zinc nitrate ($Zn(NO_3)_2$, 0.4 M) were combined in a mixed solvent system consisting of 6.66 mL of deionized water and 13.33 mL of ethylenediamine. The solution was transferred to a stainless-steel autoclave with a Teflon liner, sealed, and heated to 200°C for 16 hours. After cooling to room temperature naturally, the product was recovered by filtration and washed to remove residual reagents and ethylenediamine before being suspended in chloroform for storage and subsequent characterization. Following successful confirmation of wurtzite formation using XRD, indium doping was attempted at varying concentrations using $In(NO_3)_3$ as a precursor. Dopant concentration values of 0.05%, 0.2%, 0.5%, 1%, and 10% were used.

4.1.2 Results and Discussion

To confirm Indium incorporation into synthesized nanorods, ICP-OES was used. The results are summarized in Table 5 and show successful incorporation of the dopant at percentages close to the nominal values.

Table 5 – Nominal and Detected Indium Concentrations via ICP-OES:

Expected Indium (%)	0.05	0.20	0.50	1.00	10.00
Detected Indium (%)	0.07	0.34	0.60	0.78	8.85

Next, XRD was used to characterize all samples. Figure 10 summarizes XRD of all samples and shows the formation of wurtzite nanorods in all cases. The crystallinity decreases notably as the indium concentration increases to 10%, likely due to significant disruptions of the crystal lattice. Extraneous peaks appear at very low and very high indium concentrations. These are attributed to ethylenediaminozinc, likely due to excess organic coordinating reagents that remained on the surface of the nanocrystals.

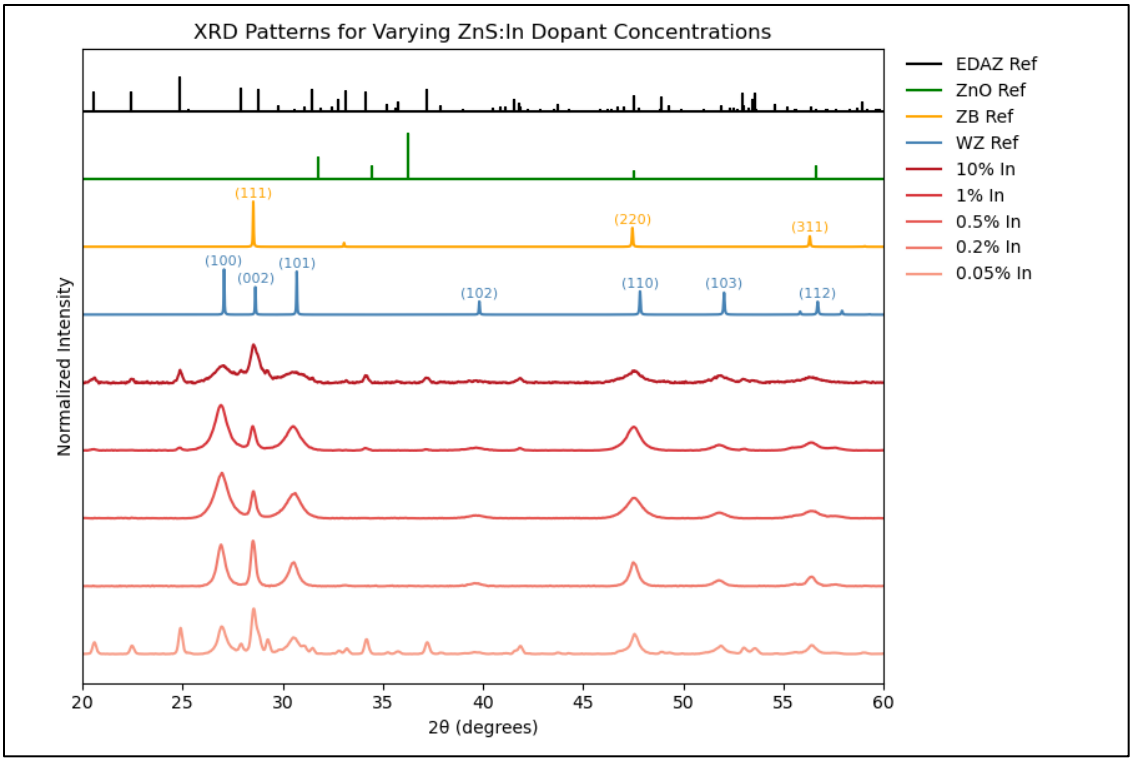

Figure 10: *XRD patterns for ZnS:In with Varying Dopant Concentrations. EDAZ is a reference pattern for ethylenediaminozinc. ZB is a reference pattern for zincblende ZnS, and WZ is a reference pattern for wurtzite ZnS.*

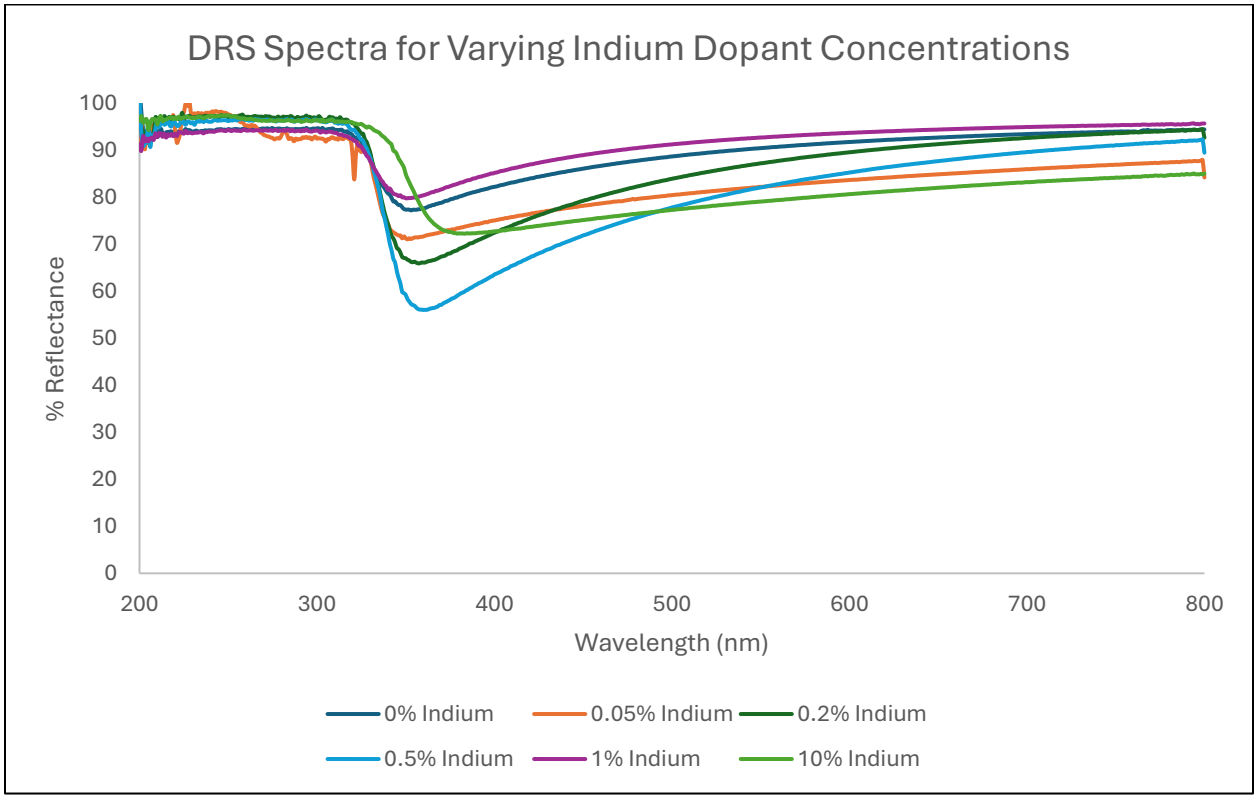

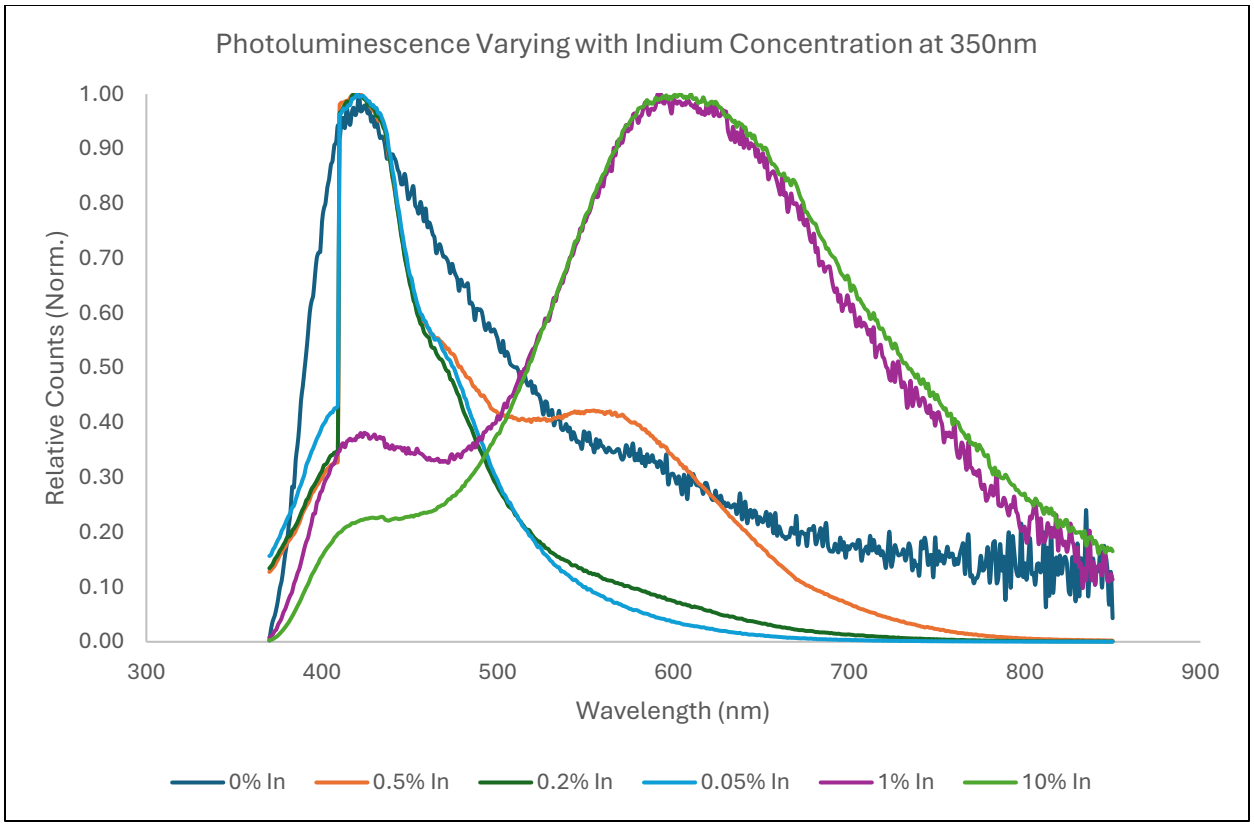

Figure 11: *Diffuse reflectance (top) and Photoluminescence (bottom) Spectra for ZnS:In with Varying Dopant Concentrations*

Figure 11 shows optical characterization of the as-made ZnS nanorods with varying indium concentration. The sharp drop in reflectance between 300-400nm corresponds to the onset of strong absorption at the ZnS bandgap, confirming the wurtzite phase with its expected bandgap of approximately 3.9 eV. The absorption onset is notably broad and red-shifted relative to the true band edge, consistent with a high density of sub-bandgap trap states. The reflectance spectrum shows a steady decrease in peak absorbance energy as the amount of In is increased. This is likely due to In^{3+} substitution at Zn^{2+} sites, causing bandgap narrowing by introducing donor states just below the conduction band. The result for the 1% dopant appears to be an anomalous result and may represent inconsistent dopant incorporation. Samples were excited at 350nm for the luminescence spectrum. The emission spectra show no band-edge emission, which would be expected at 318nm (3.91eV). The absence of any rising absorbance feature, and the emission intensity approaching zero below 380nm, indicates that band-edge emission is not a significant recombination pathway in these samples. The spectra are instead dominated by trap emission that varies wildly with the concentration of dopant. From the spectra, it appears that increasing dopant concentration shifts the emission further towards the red. The peaks at ~430nm represent native defect emission from interstitial zinc and from sulfur vacancies in the ZnS lattice (see Fig. 12). As the concentration of indium increases, the PL shifts towards 600nm, consistent with a transition from interstitial zinc to a zinc vacancy. However, some trap emission from sulfur vacancies is still observed. An increase in indium concentration is therefore creating a significant disruption in the ZnS crystal lattice and taking the place of zinc. The amount of emission from zinc vacancies seems to imply that the dopant incorporation is largely interstitial rather than substitutional. However, this cannot be decisively concluded as further characterization in the form of EPR studies would be required for confirmation.

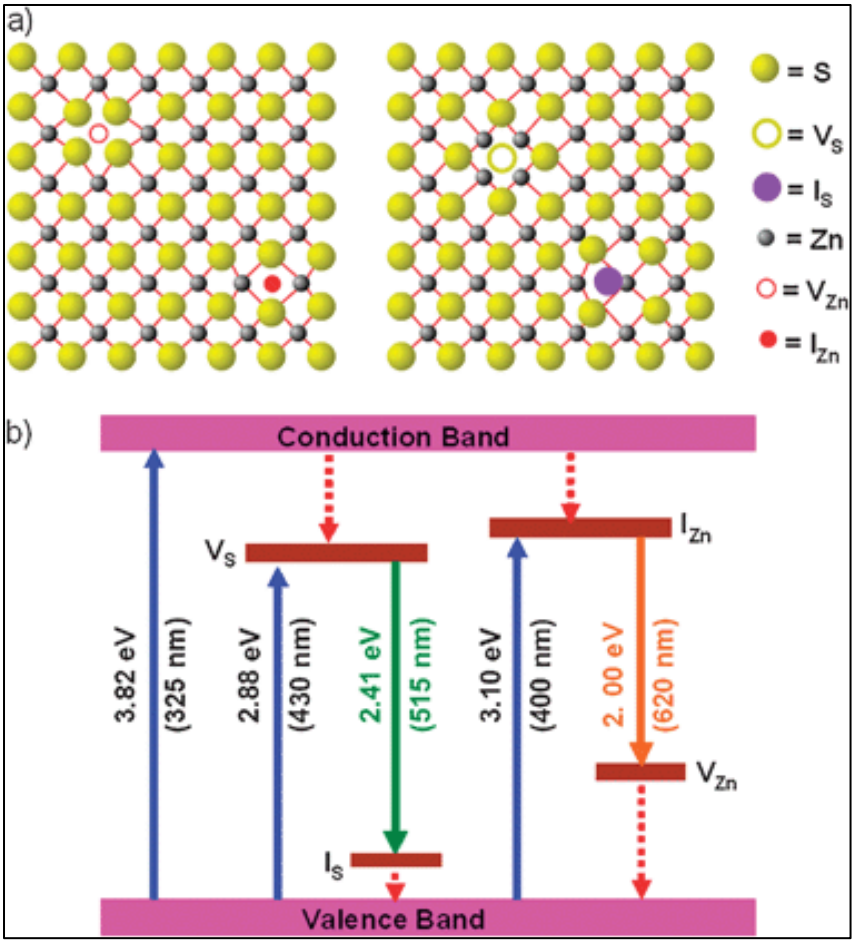

Figure 12: *Schematic of possible point defects and their energies in ZnS nanoparticles. Adapted from Wang et al. Phys. Chem. Chem. Phys., 2011, 13, 4715–4723. Copyright 2011 Royal Society of Chemistry.*[98]

To attempt to reduce the incidence of defects in the crystal lattices, a number of annealing conditions were tested in a tube furnace. The anneals were all carried out on samples with 0.2% indium and were conducted in a tube furnace at 500ºC with gas flowing through. The sulfur anneals were conducted using elemental sulfur powder. In the vacuum case, the sample and elemental sulfur were sealed inside a glass ampule under vacuum before being placed in the tube furnace. The XRD and optical characterizations are shown below:

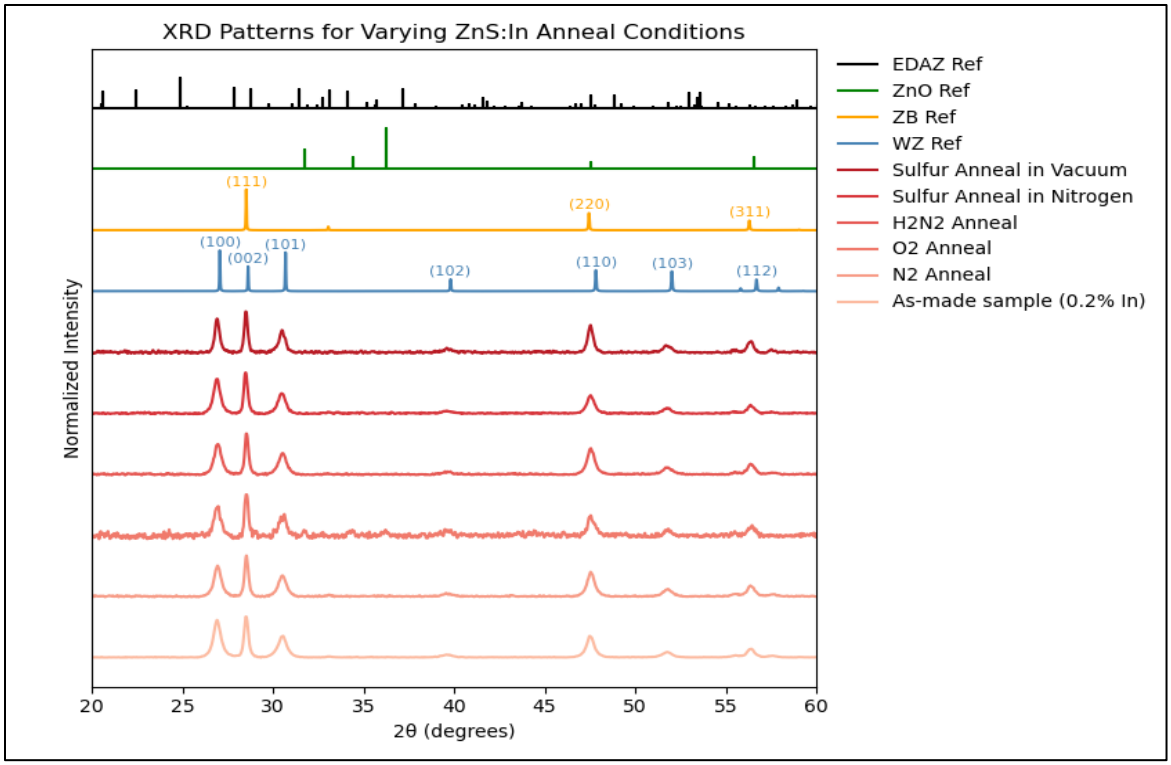

Fig 13: *XRD patterns for ZnS:In (0.2%); as made and after various anneals*

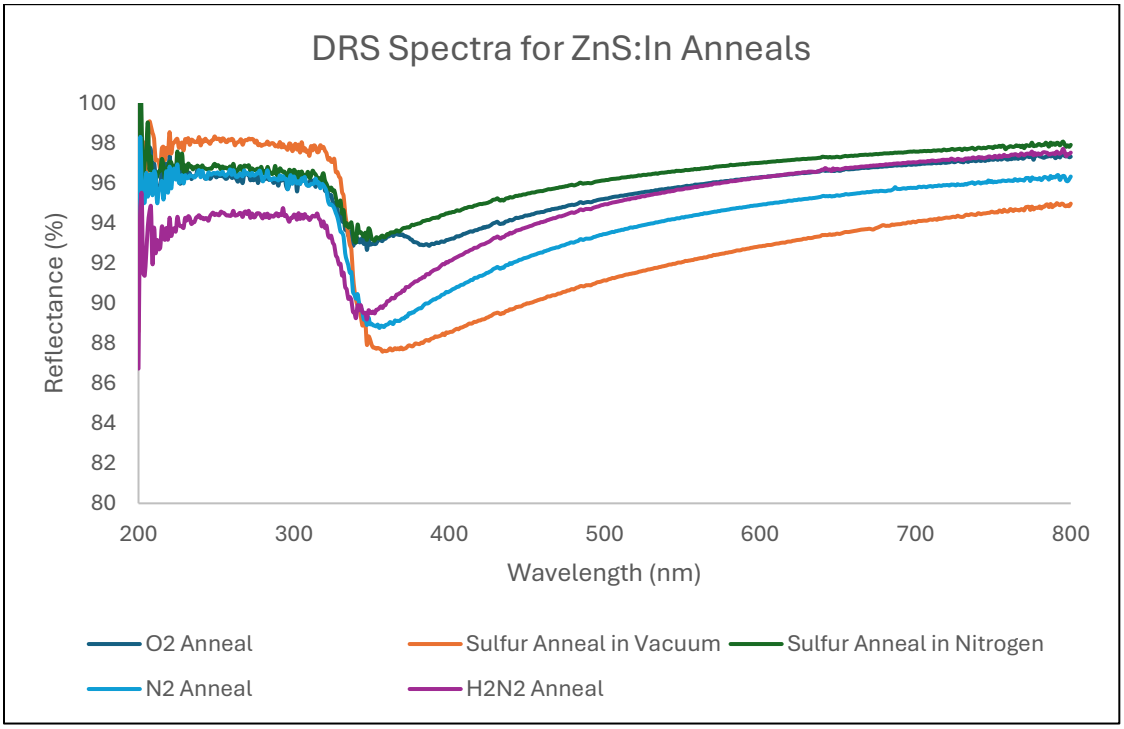

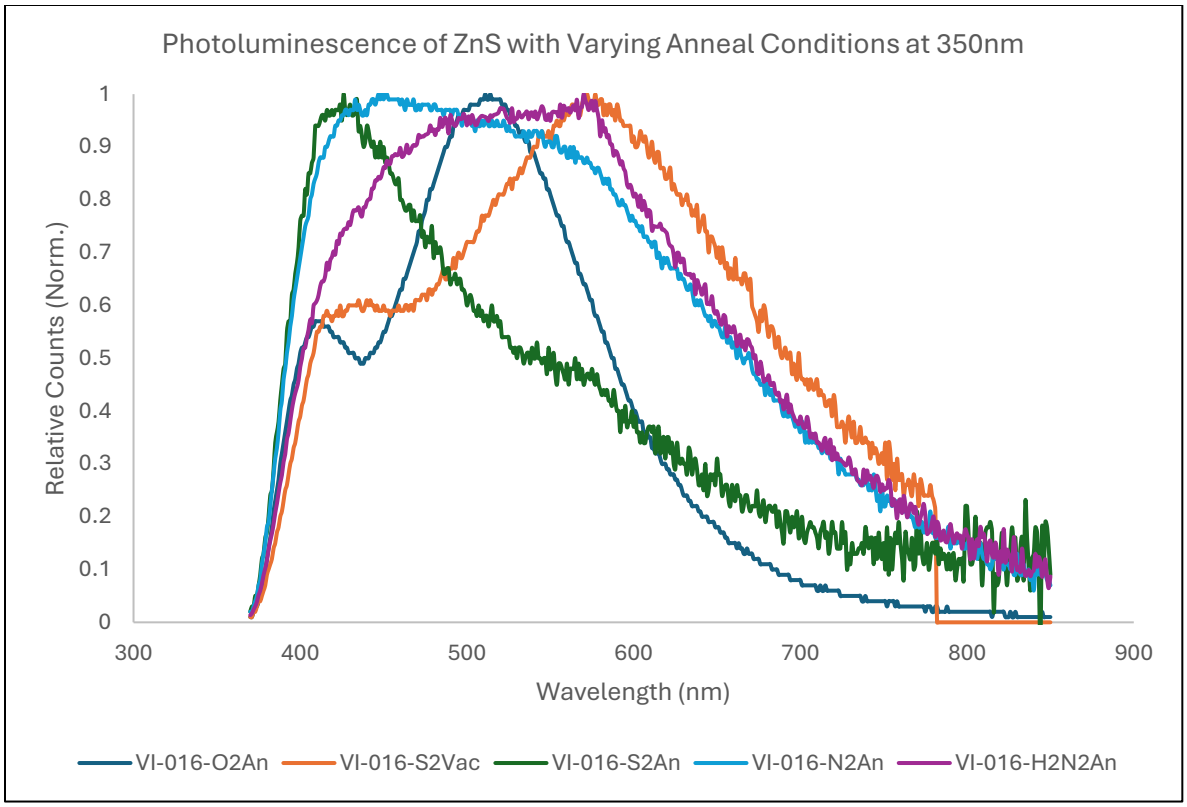

Fig 14: *Diffuse reflectance (top) and Photoluminescence (bottom) Spectra for ZnS:In after Varying Anneal Conditions*

The XRD patterns show that the crystals maintain their pure wurtzite phase after annealing. The reflectance spectrum of the oxygen annealed sample has a second peak that isn't present in other samples. This may be due to incorporation of oxygen vacancies, creating a mixture of ZnS and ZnO in the lattice. The remaining spectra are consistent with a single ZnS peak.

Photoluminescence characterization of annealed samples continues to show a large amount of defect emission. Further details are elaborated on below.

O_2 anneal (VI-016-O2An, blue): the most blue-shifted emission, peaking around 420-430 nm. Oxygen annealing passivates sulfur vacancies at the nanocrystal surface by filling or oxidizing vacancy sites, reducing the density of deep trap states responsible for longer-wavelength emission. The blue-shifted, relatively narrow emission likely represents shallower trap states or near-band-edge recombination dominating after surface oxidation.

N_2 anneal (VI-016-N2An, cyan): peaks around 460-480 nm, intermediate between O_2 and the sulfur-rich conditions. A nitrogen atmosphere is inert with respect to both oxidation and sulfurization, so the defect landscape reflects the as-synthesized nanocrystal surface without atmospheric modification. The emission is broad and relatively symmetric.

H_2/N_2 anneal (VI-016-H2N2An, purple): peaks around 500-560 nm, further red-shifted than N_2 alone. The reducing atmosphere likely introduced or preserved interstitial zinc and sulfur vacancies by preventing their oxidative passivation, increasing the density of deeper trap states, and red-shifting the emission accordingly.

Sulfur vapor anneal (VI-016-S2An, dark green): the most red-shifted and broadest emission, peaking around 500-520 nm. Sulfur annealing is expected to passivate zinc vacancy and zinc dangling bond states by providing additional sulfur to fill surface sulfur vacancies, but it can simultaneously introduce new sulfur interstitial defects.

Sulfur anneal under vacuum (VI-016-S2Vac, orange): intermediate between the sulfur and N_2 conditions, peaking around 550-580 nm with the broadest and most red-extended smooth emission profile of the series. The vacuum condition during sulfur annealing likely allows greater sulfur vapor penetration into the nanocrystal and promotes deeper restructuring of the lattice defect landscape compared to atmospheric pressure sulfur annealing, producing a higher density of deep trap emissive states and consequently the most red-shifted smooth emission.

The formation of ZnS nanorods under the given solvothermal conditions proceeds through the thermal decomposition of thiourea ($SC(NH_2)_2$) as a slow-release sulfide source, which, upon heating, hydrolyzes to release S^{2-} ions that subsequently react with Zn^{2+} from the zinc nitrate precursor to precipitate ZnS. The slow, temperature-dependent release of S^{2-} from thiourea is critical to the success of the synthesis as it suppresses instantaneous precipitation that would occur if a free sulfide source such as Na_2S were used, instead allowing a more controlled nucleation and growth process under the elevated temperature and pressure of the solvothermal environment. Ethylenediamine (en) plays a dual and closely coupled role in this process. As a bidentate ligand, it coordinates strongly to Zn^{2+} in solution to form stable $[Zn(en)]^{2+}$ complexes, effectively reducing the free Zn^{2+} activity and further slowing the rate of ZnS precipitation. Simultaneously, ethylenediamine adsorbs selectively onto the polar (0001) Zn-terminated basal facets of nascent wurtzite ZnS nuclei through coordination of its amine groups to surface zinc atoms, passivating these facets and kinetically blocking further growth in the [0001] direction.[97][99][100] This enforces preferential addition of ZnS monomer to the nonpolar $\{10\bar{1}0\}$prismatic side facets, driving elongation perpendicular to the c-axis and producing the observed nanorod morphology. The thermodynamic stabilization of the wurtzite phase over zinc blende under these conditions is also attributable in part to ethylenediamine, as the selective surface binding energy of ethylenediamine to the wurtzite (0001) facet lowers the overall surface free energy of the wurtzite polymorph relative to zinc blende, shifting the phase stability in favor of the otherwise metastable wurtzite structure at the nanoscale. The presence of water in the mixed solvent system, however, introduces a competing reaction pathway that is likely responsible for the broad defect-mediated emission observed in the optical spectra. Water can participate in the hydrolysis of both thiourea and the $[Zn(en)]^{2+}$ complex, generating hydroxide ions that compete with S^{2-} for coordination to Zn^{2+} surface sites and potentially incorporating oxygen-containing species, such as Zn-OH surface groups or ZnO inclusions, into the growing nanocrystal.[61][101] These surface species introduce a heterogeneous defect landscape at the nanocrystal surface, producing the broad distribution of sub-bandgap trap states that manifest as the wide, featureless emission spanning 370–800 nm observed across all annealing conditions. Furthermore, water molecules coordinated to surface zinc sites can act as non-radiative recombination centers by introducing mid-gap hydroxyl-related states, and their presence would likely contribute to the suppression of any sharp donor-bound exciton emission from In^{3+} that might otherwise be observable at low temperatures.[61] Reducing the water content of the solvent system was therefore hypothesized to be a productive direction for improving the optical quality of In-doped ZnS nanorods produced by this route. To this end, the synthesis was adapted, after some experimentation, to use dimethylformamide (DMF) as a replacement solvent, as discussed in the next section.

4.2 Air-free synthesis leading to $ZnS(en)_{0.5}$

To address the defect formation attributed to water incorporation identified in the initial solvothermal synthesis, a modified air-free, water-free synthetic protocol was developed in which water was replaced entirely by anhydrous DMF as co-solvent. DMF was selected as a water replacement on the basis of its high boiling point, miscibility with ethylenediamine, compatibility with the solvothermal conditions employed, and its aprotic character; unlike water, DMF cannot donate protons to generate hydroxide species or participate in competing hydrolysis reactions at the nanocrystal surface during growth. Prior to use, both DMF and ethylenediamine were degassed and dried by distillation *in vacuo* to remove residual water. Solid precursors zinc acetate, indium nitrate,

and thiourea were dried overnight under vacuum and by heating to 95°C. All reagents were then transferred into a nitrogen-filled glovebox. All subsequent synthetic manipulations, including precursor weighing, dissolution, and autoclave loading, were carried out inside the glovebox under rigorously inert conditions to prevent water or oxygen exposure. The nominal In^{3+} doping level was set at 0.2 mol% relative to Zn^{2+} (0.3992 M $Zn(NO_3)_2$ and 0.0008 M $In(NO_3)_3$) with thiourea maintained at 1.2 M, dissolved in 6.66 mL of dry DMF and 13.33 mL of dry ethylenediamine. Sealed autoclaves were removed from the glovebox and heated at 200°C for 16 hours under nitrogen, replicating the thermal conditions of the original synthesis. To evaluate the impact of post-synthetic air and moisture exposure on the optical properties of the product, the reaction was run in duplicate, with one sample worked up entirely within the glovebox under inert atmosphere, filtered, and suspended in dry DMF, while the second was worked up identically but under ambient laboratory conditions. Rather than washing with water and acetone as before, the samples were instead washed with anhydrous DMF and anhydrous acetonitrile to remove unreacted precursors and impurities. Both products were vacuum dried before storage. This alternative workup allows the contribution of post-synthetic oxidation and surface hydroxylation to the defect emission observed in earlier samples to be isolated from defects introduced during the synthesis itself, providing a more complete picture of the origins of the broad trap-state emission and informing whether inert handling at the workup stage is necessary in addition to anhydrous synthesis conditions. The samples' absorbances were measured using diffuse reflectance spectroscopy, then the Kubelka-Munk transform was applied to create the absorbance spectra shown below. Accordingly, photoluminescence spectra were also taken.

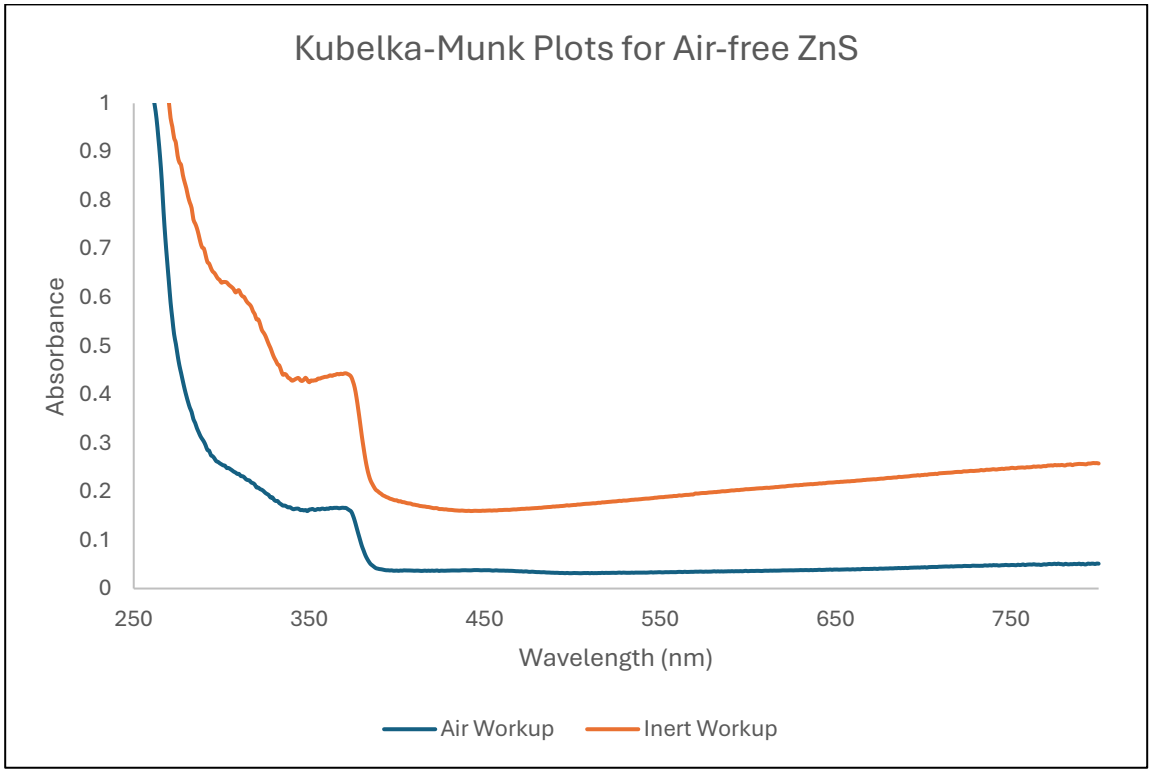

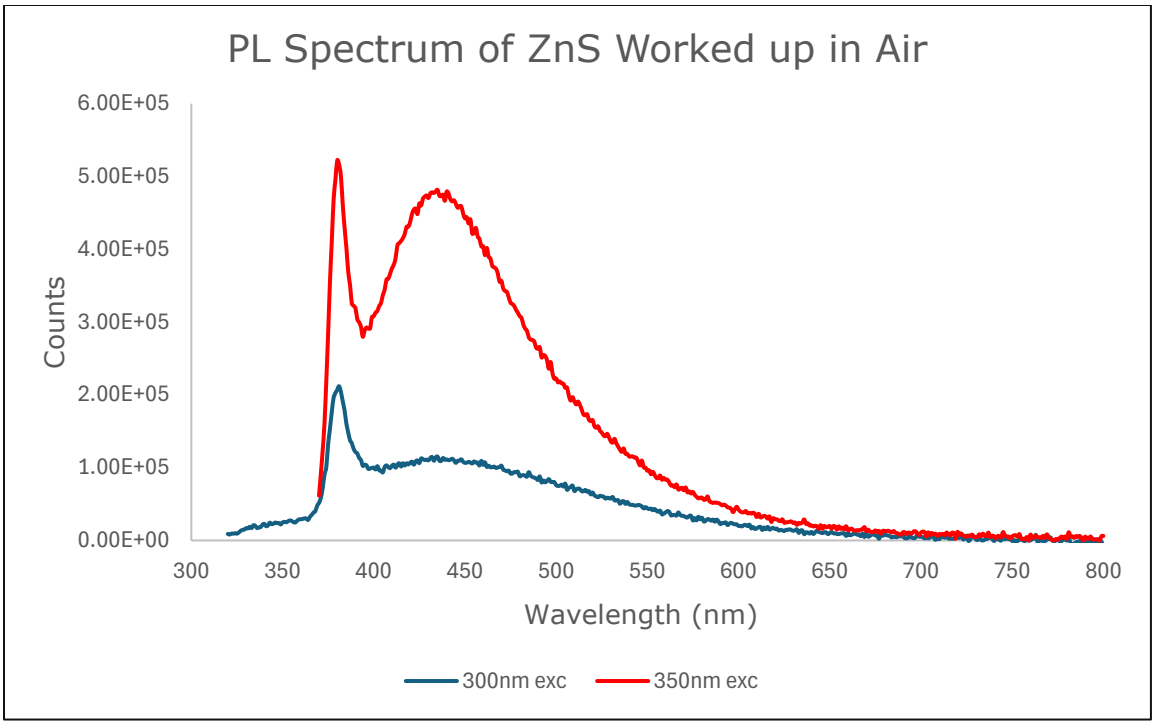

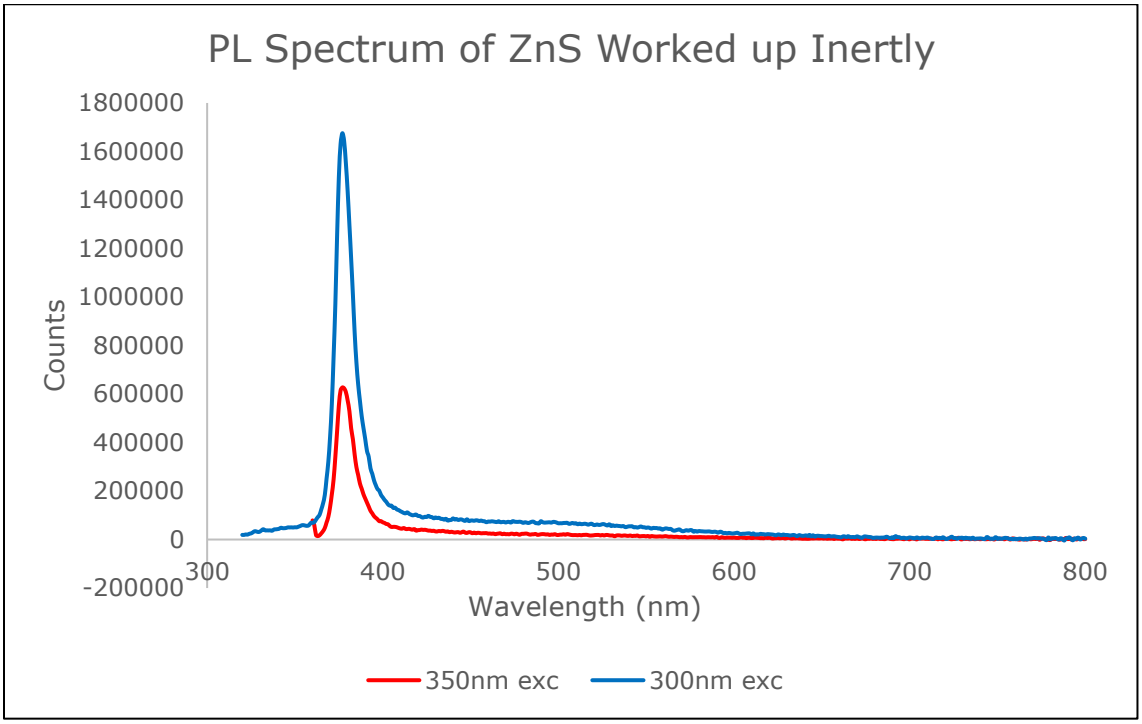

Fig 15: *From top to bottom – Kubelka-Munk plots for air-free ZnS worked up inertly and in air, photoluminescence spectra for air-free ZnS worked up in air, photoluminescence spectra for air-free ZnS worked up inertly. PL spectra are provided for excitations at both 300 nm and 350 nm.*

The Kubelka-Munk plots both show absorbance features at 314 and 375 nm. The former peak appears to be consistent with a ZnS band edge at ~3.91 eV, while the latter appeared to show intermediate states.

Photoluminescence spectra for the sample worked up inertly show a significant feature at 377nm with a small tail, indicating some trap emission. The full-width half max (FWHM) of the emission spectrum when excited at 350 nm is 101 meV; when excited at 300 nm it is 103 meV. This is comparable to typical ensemble CdSe emission at room temperature, which has a reported FWHM of 111 meV.[102] Photoluminescence spectra for the sample worked up in air show an assumed band-edge feature at 381nm, while showing significantly more trap emission centered at 437nm. This suggests that ambient water and oxygen continue to impact the surface of the nanocrystals even after the solvothermal process is complete. However, in both cases, emission is significantly improved compared to non-air-free syntheses. At first glance, the data seemed to show the formation of ZnS with strong band-edge emission features and low trap emission when the precipitate is worked up inertly. To test this further, structural XRD and TEM characterizations were conducted. X-ray photoelectron spectroscopy (XPS) was also performed to confirm the oxidation states of the constituent elements and check for In^{3+} incorporation:

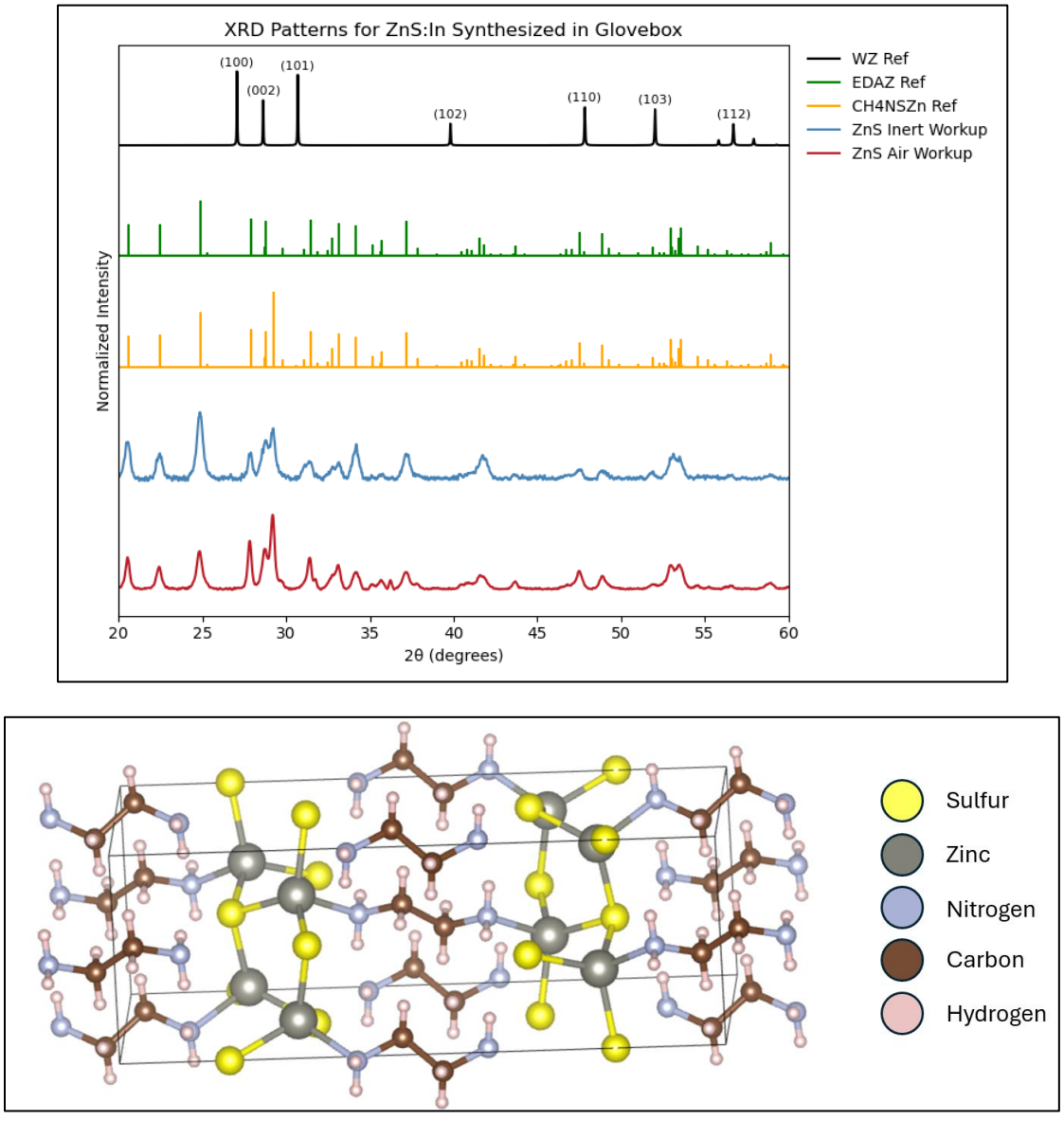

Figure 16: *XRD patterns for ZnS synthesized in glovebox, and literature structure corresponding to CH_4NSZn reference spectrum.*

XRD patterns do not support prior assertions based on the optical spectra. Rather than wurtzite phase ZnS, both syntheses show the formation of CH_4NSZn as labeled. The shown reference spectrum corresponds to the structure shown. It is a bridged structure where sheets of ZnS are bound to ethylenediamine via the amines on either end. In previous syntheses, ethylenediaminozinc was formed when ZnS was doped at high concentrations. However, that impurity and the presently formed bridged structure are distinguished by an XRD peak at 29.2°, which is seen in both the current samples, but not in prior ones. In addition, reported photoluminescence spectra

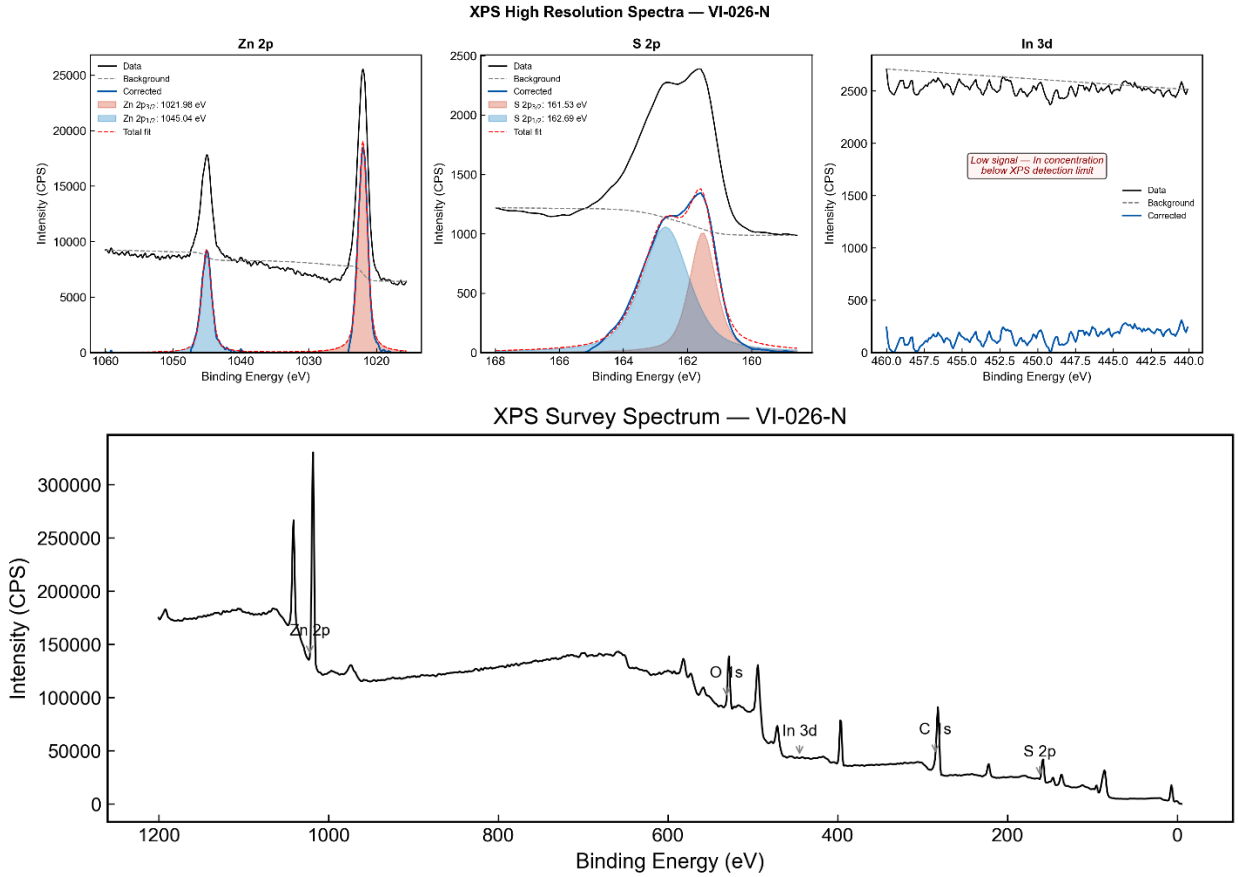

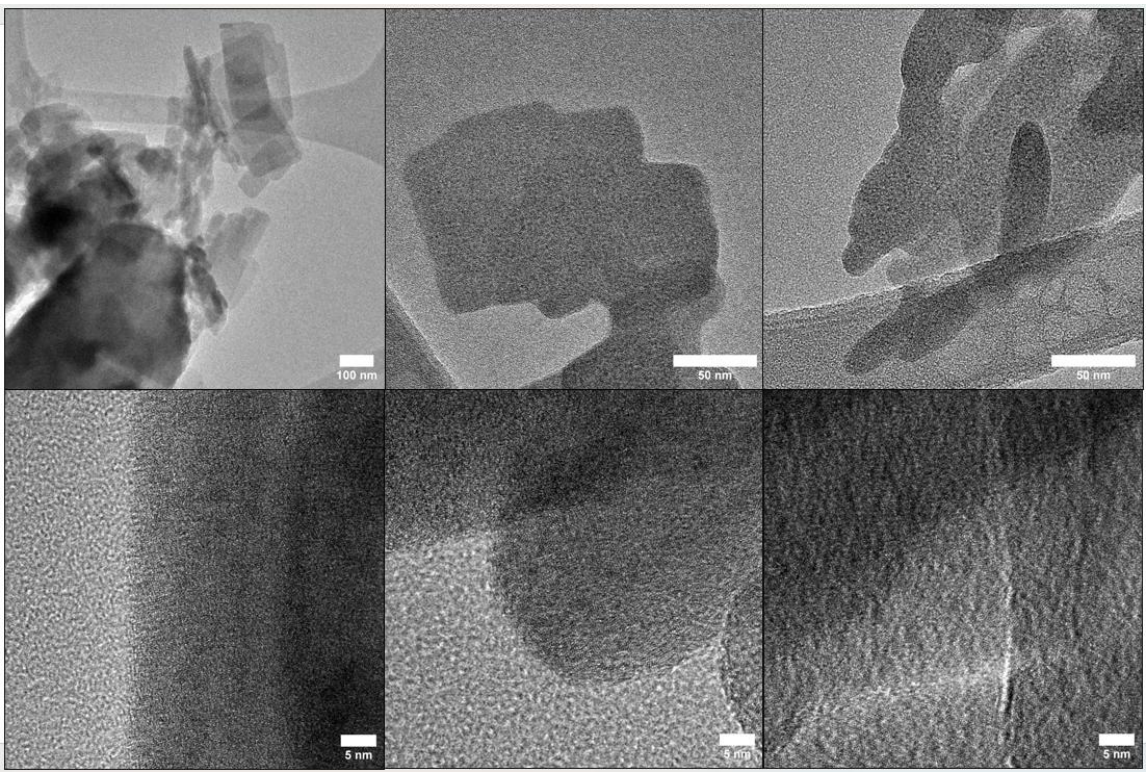

Figure 17: *X-ray photoelectron spectra and representative TEM, HRTEM images; only for the ZnS sample worked up in the glovebox.*

The XPS survey spectrum confirmed the presence of Zn and S as the primary constituents, alongside adventitious carbon (C 1s, ~284.8 eV) and surface oxygen (O 1s, ~531 eV), both of which are ubiquitous surface contaminants arising from atmospheric exposure and do not indicate the presence of bulk impurity phases. The presence of surface oxygen species is likely also from atmospheric contamination post-workup. High resolution Zn 2p spectra revealed doublet peaks at 1021.98 eV (Zn $2p_{3/2}$) and 1045.04 eV (Zn $2p_{1/2}$), giving a spin-orbit splitting of 23.1 eV in good agreement with literature values for Zn^{2+} in a sulfide environment, and clearly distinct from the binding energy expected for ZnO (~1022.5 eV) or metallic zinc (~1021.1 eV). High resolution S 2p spectra showed doublet peaks at 161.53 eV (S $2p_{3/2}$) and 162.69 eV (S $2p_{1/2}$) with a spin-orbit splitting of 1.16 eV, consistent with S^{2-} in a zinc sulfide environment and excluding the presence of sulfate (~168 eV) or elemental sulfur (~164 eV) as secondary phases. No In 3d signal above the noise floor was detected in either the survey spectrum or the high-resolution scan, likely a consequence of the low nominal doping concentrations employed.

HRTEM of the inert synthesis product shows a hierarchical assembly mechanism underlying the formation of the observed plate-like morphology. At the nanoscale, the material consists of small primary crystalline domains, visible as discrete circular regions with well-defined lattice fringes, each about 2 nm in diameter, as estimated from the images. These primary domains are not ZnS nanocrystals passivated by surface-bound ethylenediamine ligands. They instead represent nuclei of the ZnS·en hybrid phase, in which ethylenediamine is incorporated as a structural component of the crystal lattice from the very first moment of nucleation.[103] This occurs because under the solvothermal conditions employed, Zn^{2+} coordinates simultaneously to both S^{2-} ions released by the thermal decomposition of thiourea and to the nitrogen donor atoms of ethylenediamine, producing the hybrid phase directly rather than first forming pure ZnS and subsequently adsorbing organic ligands onto its surface. The thermodynamic driving force for hybrid phase formation over pure wurtzite ZnS is strong under these conditions, particularly at the high ethylenediamine concentrations employed here, where the organic component constitutes the majority of the

solvent volume. The primary ZnS·en crystallites subsequently assemble into the larger plate-like structures observed at lower magnification through a bridging mechanism. The surface zinc atoms of each primary crystallite have unbound sites that can be bridged by either free ethylenediamine molecules in solution or by the surface-exposed ethylenediamine units of adjacent crystallites, thereby connecting neighboring domains together. Because the ethylenediamine bridge is a short, geometrically constrained two-carbon chain with amine donors at each terminus, this bridging occurs preferentially in specific crystallographic directions enforced by the ligand geometry, creating lateral 2D sheets rather than 3D aggregation. The distinct crystallographic orientations within individual primary domains are evidenced by the overlapping and non-parallel lattice fringe directions visible throughout the HRTEM images and confirm that the sheet formation process does not involve complete crystallographic re-ordering into a single crystal but rather the connection of the primary structures formed during initial nucleation. These observations suggest that, without water as a competing binder and hydrolyzer, the high ethylenediamine concentration is able to compete with the sulfur atoms more effectively.

Following this finding, the luminescence spectra also need to be reinterpreted. The photoluminescence spectrum of the inertly-worked-up sample exhibits a sharp emission feature at 377nm. The narrow linewidth and complete insensitivity of both peak position and linewidth to post-synthetic water exposure strongly suggest this is an intrinsic band-edge transition of the ZnS·en hybrid phase rather than a surface or defect state. The red-shift of approximately 50nm relative to band-edge emission reported for ZnS·en nanobelt structures (~327nm) may reflect differences in hybrid phase composition, layer spacing, or organic content between samples, all of which can modify the effective bandgap of organic-inorganic hybrid semiconductor materials.[104][105] Confirmation of the intrinsic nature of this transition and its precise assignment would require low-temperature PL measurements and systematic variation of the ethylenediamine content.

To isolate the role of ethylenediamine in directing the phase and optical properties of the solvothermally synthesized ZnS products, three additional reactions were conducted under the same inert, water-free conditions using the anhydrous DMF synthesis protocol established. The three conditions were synthesis in the absence of any amine, synthesis with oleylamine as a monoamine analogue, and a repeat synthesis with ethylenediamine as a control.

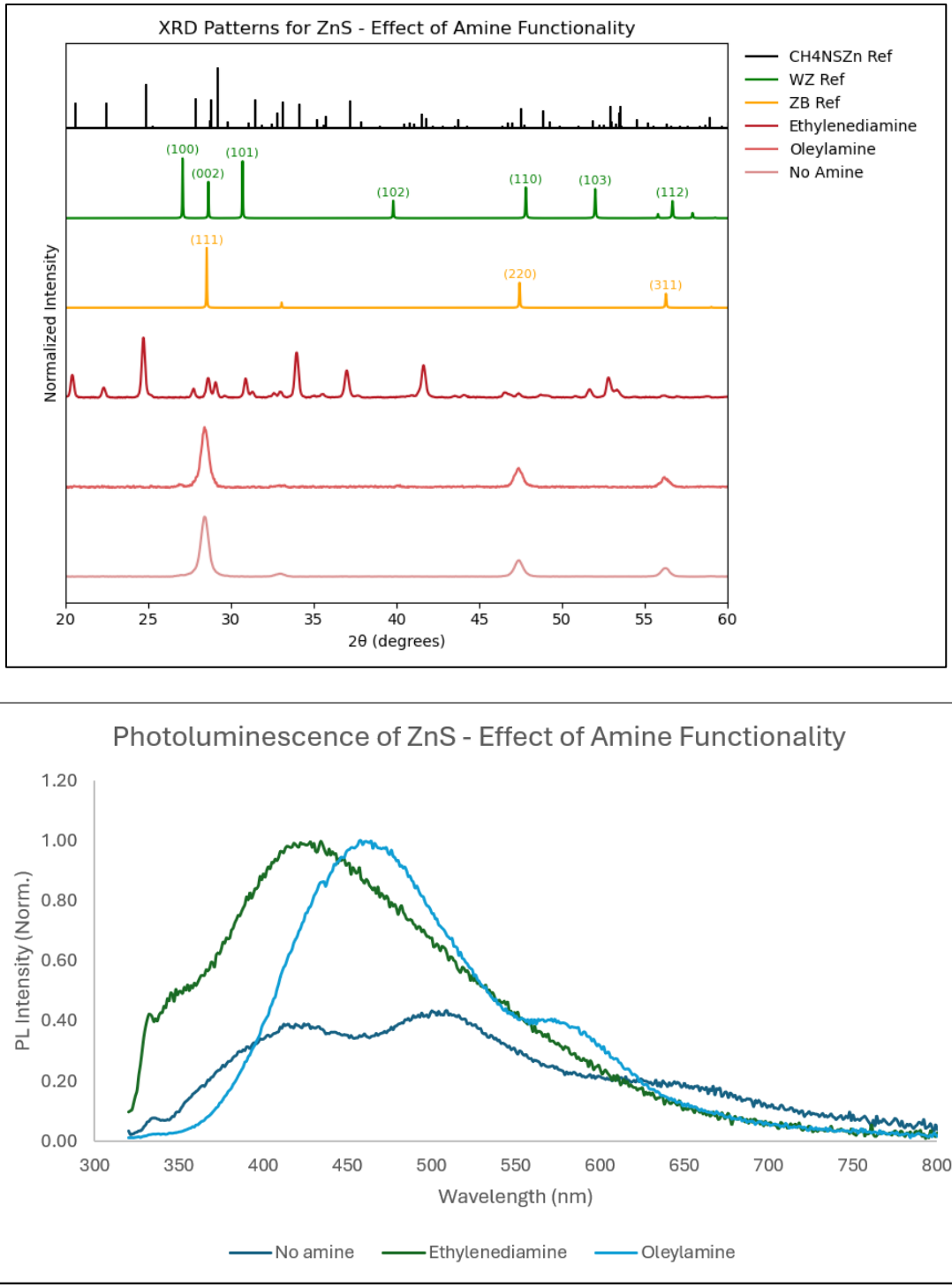

Figure 18: *XRD patterns and luminescence spectra (300 nm exc.) for solvothermal reactions investigating the effect of amine functionality on ZnS phase formation. Conditions compared are no amine, monoamine (oleylamine), and diamine (ethylenediamine).*

XRD analysis of the amine-free and oleylamine products confirm formation of the thermodynamically favorable zinc blende phase of ZnS in both cases. The ethylenediamine repeat confirmed the hybrid phase as established previously. These results demonstrate that the bidentate coordination geometry of ethylenediamine, not

the presence of an amine functional group, is the critical factor driving hybrid phase formation. Oleylamine, despite bearing a terminal amine group, functions only as a monodentate surface ligand and cannot bridge between adjacent zinc centers to form the structural component of the hybrid lattice. This represents direct experimental evidence for the bridging mechanism proposed for ZnS·en formation, and is consistent with the structural chemistry reported by Han et al. and Yu et al.[106]

The photoluminescence spectra of the amine-free and oleylamine samples revealed a striking difference in emission intensity despite their identical crystal structures. The oleylamine-passivated sample exhibited substantially higher PL intensity with emission centered around 450nm, while the unpassivated amine-free sample produced broader, weaker emission red-shifted toward 500nm. This observation suggests that oleylamine surface passivation reduces the density of non-radiative surface trap states without altering the bulk crystal structure, which is consistent with the known role of long-chain amine ligands in passivating surface zinc dangling bonds in II-VI nanocrystals.[61] The persistence of broad defect-dominated emission in both samples, with no observable band-edge emission, is attributed in part to residual water contamination of the DMF solvent used in these reactions. The DMF used for these experiments was not properly purified prior to synthesis, whereas the DMF used for prior experiments was properly distilled.

A fourth experiment was also conducted, in which the ZnS·en hybrid product from this section's initial synthesis was redispersed in DMF and subjected to identical solvothermal conditions to investigate thermally driven conversion of the hybrid phase.

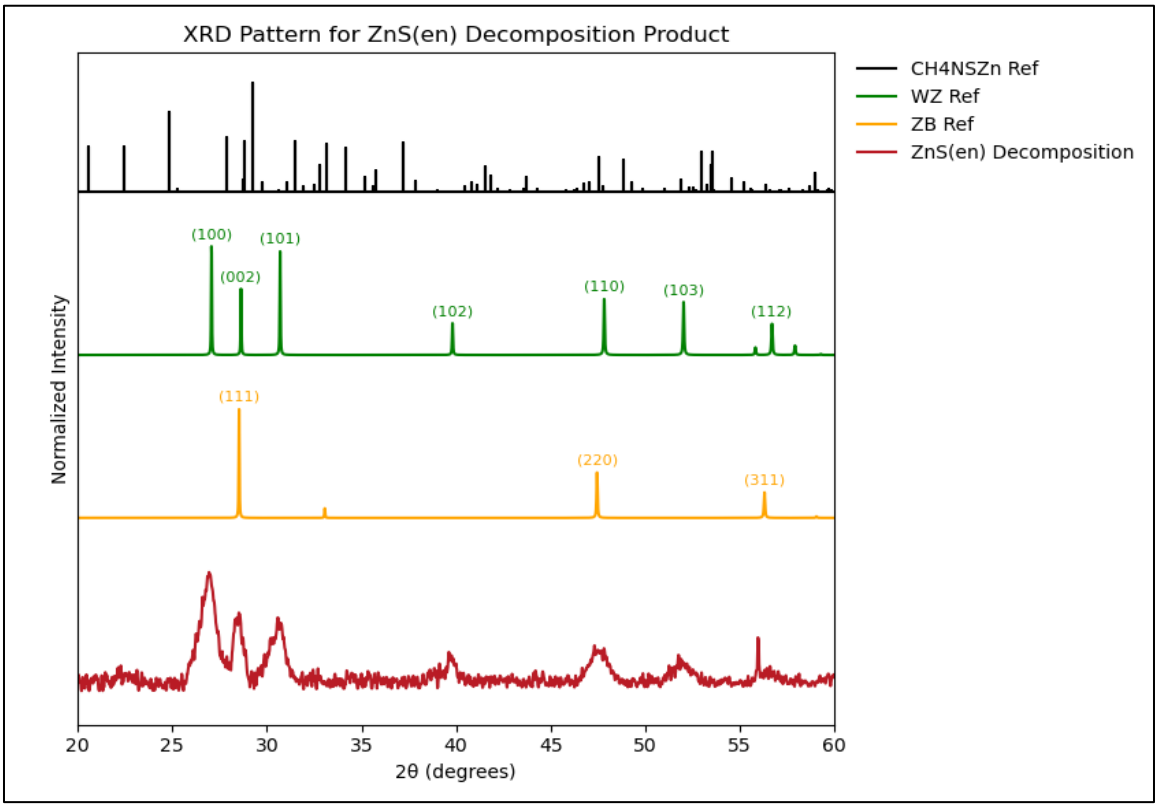

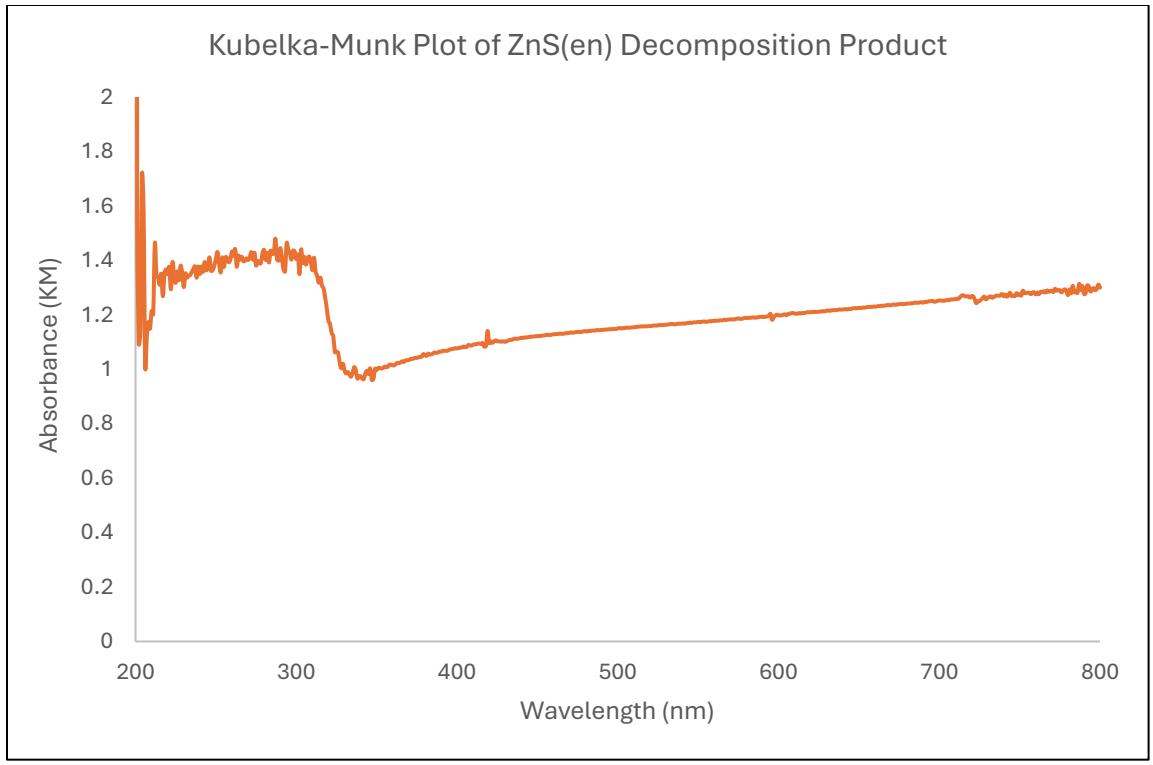

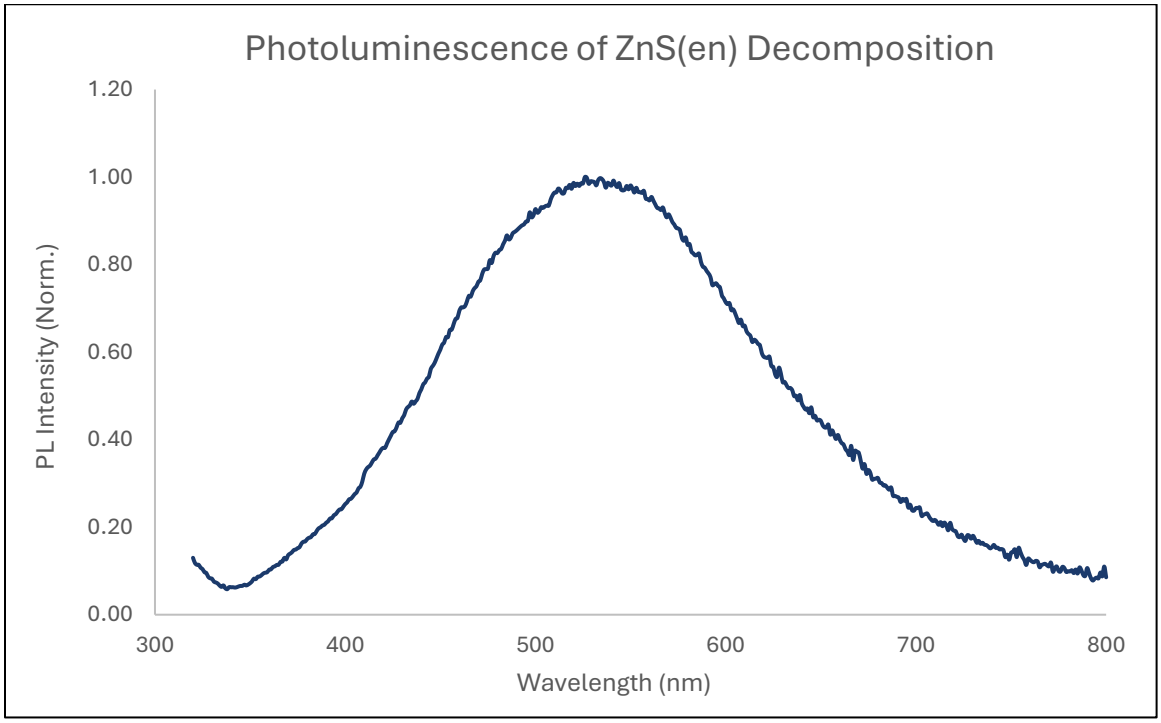

Figure 19: *XRD pattern and optical spectra for ZnS(en) decomposed in DMF.*

The seeded decomposition experiment, in which pre-formed ZnS·en hybrid was redispersed in DMF and subjected to solvothermal treatment at 200°C, produced a product whose XRD pattern is consistent with the wurtzite phase of ZnS, with peaks aligning with the wurtzite reference at approximately 28°, 33°, and 47° 2θ and without the

additional low-angle reflections characteristic of the hybrid phase. This suggests that solvothermal treatment in DMF at 200°C is sufficient to drive partial or complete removal of the structurally incorporated ethylenediamine from the hybrid lattice, converting the ZnS·en precursor to wurtzite ZnS. This is a lower-temperature solution-phase analogue of the thermal decomposition route reported by Yu et al. at 350°C under inert gas.[106] The crystallinity of this wurtzite product appears to be lower than that of those synthesized previously in this study, as the peaks in the XRD pattern are much broader than those of the In-doped ZnS nanorods formed earlier. Importantly, the Kubelka-Munk plot shows an absorbance feature at 317 nm, which corroborates the structure as wurtzite ZnS with an estimated bandgap of 3.91eV. The photoluminescence of the decomposed product shows broad emission centered around 520-540nm, red-shifted relative to the zinc blende samples, which is again attributed to the water-contaminated DMF introducing surface hydroxyl defects during the decomposition step rather than reflecting an intrinsic property of the wurtzite product. The broad symmetric emission peak and featureless KM absorption profile are consistent with a high density of sub-bandgap trap states in the decomposed product, likely arising from a combination of residual organic species from incomplete ethylenediamine removal and water-derived surface defects. Further testing is required to identify whether the amine can still be removed in anhydrous conditions or if hydrolysis is the main driver of this decomposition.

Taken together, these four experiments establish three important conclusions. First, that bidentate amine coordination is a necessary condition for ZnS·en hybrid phase formation under these solvothermal conditions; second, that monoamine surface passivation can improve the optical quality of zinc blende ZnS nanocrystals without altering their crystal structure; and third, that the ZnS·en hybrid phase can be converted to wurtzite ZnS by solvothermal treatment in DMF, potentially offering a lower-temperature solution-phase route to phase-pure wurtzite ZnS if water contamination can be fully eliminated. The optical properties of all samples in this series were adversely affected by DMF water contamination, underscoring the critical importance of rigorous solvent drying in future work and motivating further investigation under fully anhydrous conditions.

5. Conclusions and Future Directions

This thesis has pursued the synthesis of doped zinc chalcogenide nanocrystals as candidate host materials for optically addressable defect states relevant to quantum information science. Three distinct synthetic thrusts were undertaken across two host material systems, ZnO and ZnS, each targeting a different dopant strategy and motivated by the complementary optical and spin properties of the intended dopant states. While none of the synthetic thrusts achieved their ultimate objective of producing a material with the optical quality required for quantum optical measurements, each produced meaningful results that advance the understanding of the synthetic challenges involved and suggest productive directions for future work.

The first synthetic thrust targeted the production of homogeneous In-doped ZnO nanorods by alkaline hydrolysis of zinc acetate in ethanol. Despite systematic variation of reaction temperature, time, precursor concentration, base identity, and addition rate, as well as attempts at oriented attachment using pre-formed spherical ZnO seeds, the synthesis consistently produced oblate or quasi-spherical nanocrystals rather than the desired anisotropic nanorods. The wurtzite crystal structure was confirmed by XRD in all cases, demonstrating phase purity but not morphological control. The failure to achieve rod morphology by this route is attributed to the absence of selective facet-capping agents that would direct growth along the c-axis, and to the temperature limitations of the ambient-pressure ethanol system. These results establish that the alkaline ethanol route, while useful for producing phase-pure wurtzite ZnO nanocrystals, is likely not a suitable platform for reliable nanorod synthesis without the addition of structure-directing agents such as polyethylenimine or cetyltrimethylammonium bromide.

The second synthetic thrust investigated the use of pre-formed $Ti_8Yb_2O_{12}(PhCOO)_{16}$ heterometallic clusters as seeds for ZnO shell growth, targeting Yb^{3+} deep donor states with near-infrared emission at ~980 nm. Synthesis in both DMA and DMSO produced ZnO-containing products as confirmed by XRD and near-band-edge PL features, but neither produced the well-defined core-shell morphology required for Yb^{3+} incorporation. The absence of Yb^{3+}

emission at 980 nm in both solvents indicates that either Yb was not incorporated, or that energy transfer from the ZnO host to the Yb^{3+} centers was not achieved, likely due to the failure of ZnO shell nucleation on the cluster surface in competition with homogeneous ZnO nucleation in solution. The DMSO synthesis produced nanocrystals with notably lower trap emission than the DMA synthesis, attributed to the stronger coordinating character of the sulfoxide oxygen providing more effective surface passivation.

The third and most extensive synthetic thrust pursued the synthesis of In-doped ZnS nanorods by solvothermal methods, using ethylenediamine as a structure-directing agent. Initial water-based solvothermal synthesis successfully produced wurtzite ZnS nanorods with confirmed In^{3+} incorporation by ICP-OES across a range of doping concentrations from 0.05% to 10%. Optical characterization revealed systematic bandgap narrowing with increasing In^{3+} concentration, consistent with shallow donor state formation, but all samples were dominated by broad defect-mediated emission attributed to various intrinsic defects exacerbated by the aqueous synthetic conditions. A systematic annealing study across five atmospheres demonstrated that the defect landscape of the ZnS nanorods is highly sensitive to post-synthetic treatment, with oxygen annealing producing the most blue-shifted emission consistent with shallower trap states, and reducing or sulfur-rich atmospheres producing progressively red-shifted emission consistent with deeper vacancy states.

The development of a water-free, air-free synthesis using anhydrous DMF as co-solvent produced materials with dramatically improved optical properties. Narrow emission with FWHM of ~101 meV comparable to best-in-class CdSe quantum dots at room temperature was achieved. However, XRD characterization revealed that the product was a ZnS·en hybrid phase rather than the intended pure wurtzite ZnS. HRTEM imaging and systematic investigation of amine functionality established that the bidentate coordination geometry of ethylenediamine is the critical factor driving hybrid phase formation, with monoamine analogues producing zinc blende ZnS under otherwise identical conditions. Crucially, solvothermal treatment of the pre-formed ZnS·en hybrid in DMF at 200°C produced a product consistent with wurtzite ZnS by XRD, demonstrating a lower-temperature solution-phase conversion route that may represent a viable path to pure wurtzite ZnS if conducted under fully anhydrous conditions. This finding reframes what initially appeared as a synthetic failure into a potentially useful two-step synthetic strategy.

Several directions for future work emerge from these results. First, the conversion of ZnS·en to wurtzite ZnS should be repeated under fully anhydrous conditions to determine whether water is the primary driver of ethylenediamine removal or whether the conversion can proceed thermally without hydrolysis. ICP-OES data should also be collected on this species to test for dopant incorporation. If In is not identified in ICP data, then In^{3+} doping should be attempted during or after the hybrid-to-wurtzite conversion step, rather than during the initial hybrid formation, to test whether substitutional In^{3+} incorporation is more accessible in this two-step route than in the direct solvothermal synthesis. Third, the amine-free and oleylamine-passivated zinc blende ZnS products identified in the amine functionality study represent a potentially cleaner platform for In^{3+} doping in the absence of the hybrid phase complication. The simpler crystal structure and well-passivated surface of the oleylamine-capped zinc blende product may facilitate characterization of In^{3+} donor states without the interference of ethylenediamine-related phases, though it may complicate the formation of nanorod morphology. Fourth, recreation of the ZnS·en structure should be reattempted using propylenediamine and 1,4-diaminobutane in order to test whether the band-edge peak seen with ethylenediamine shifts. A decomposition experiment on these products in DMF could also have an impact on crystallinity and phase of the resulting ZnS nanocrystals. Fifth, the cluster shelling approach for Yb^{3+} incorporation warrants further investigation with new synthetic approaches, potentially involving coordinating agents to direct nucleation on the cluster rather than extraneously. Finally, all materials identified as promising candidates in this study require low-temperature PL characterization, as the donor-bound exciton transitions that motivate the entire research program are only observable at cryogenic temperatures and cannot be assessed from the room-temperature measurements reported here. The synthesis of materials with sufficient optical quality to support these measurements remains the central challenge and the most important objective for future work in this area.

6. Acknowledgements

I would like to extend my sincere thanks to the Department of Chemistry at the University of Washington, and to the many individuals who have supported my journey towards the completion of this thesis.

I would especially like to thank my research advisor, Prof. Brandi Cossairt. Her detailed guidance, patience, and mentorship have helped me grow as a student, scientist and person. I have learned a great deal more than I imagined I would when I joined this program, and the welcoming atmosphere created by her and her lab were central to my development in this regard. I am truly fortunate to have had her mentorship. I would like to thank the other members of the Cossairt lab for their support and guidance during the course of my degree. Entering the lab with limited experience in this field, I relied greatly on their mentorship and willingness to answer questions large and small alike.

Additionally, I would like to thank my friends, in Seattle and around the world, for their lasting companionship, encouragement, and support.

Finally, I want to thank my family, especially my parents, sister, and my relatives in the Seattle area. Your unwavering love, support, and belief in me helped me complete this journey despite moments of doubt. It is a rare gift to feel at home on the both sides of the world, and I owe this journey and accomplishment to you.

7. References

(1) Haq, F. ul; Batool, A.; Niazi, S.; Khan, I. M.; Raza, A.; Ali, K.; Yang, J.; Wang, Z. Doped Magnetic Nanoparticles: From Synthesis to Applied Technological Frontiers. *Colloids and Surfaces B: Biointerfaces* **2025**, *247*, 114410. https://doi.org/10.1016/j.colsurfb.2024.114410.

(2) Javed, F.; Abbas, M. A.; Asad, M. I.; Ahmed, N.; Naseer, N.; Saleem, H.; Errachid, A.; Lebaz, N.; Elaissari, A.; Ahmad, N. M. Gd3+ Doped CoFe2O4 Nanoparticles for Targeted Drug Delivery and Magnetic Resonance Imaging. *Magnetochemistry* **2021**, *7* (4), 47. https://doi.org/10.3390/magnetochemistry7040047.

(3) Olusegun, S. J.; Osial, M.; Agnieszka Majkowska-Pilip; Kinga Żelechowska-Matysiak; Dorota Nieciecka; Krajewski, M.; Marek Pękała; Krysinski, P. Synthesis and Characterization of Sr2+ and Gd3+ Doped Magnetite Nanoparticles for Magnetic Hyperthermia and Drug Delivery Application. *Ceramics International* **2023**, *49* (12), 19851–19860. https://doi.org/10.1016/j.ceramint.2023.03.102.

(4) Hosny, A. A.; El-Deeb, B.; Mohamed, Z. A.; Hassan, A.; Kamel, M.; Elbeltagi, S.; Saadallah, H. A. A.; Ibrahim, E. M. M. Green Synthesis of Mn-Doped Iron Oxide Nanoparticles Using Sugarcane Juice for Magnetic Hyperthermia Applications. *Scientific Reports* **2025**, *15* (1). https://doi.org/10.1038/s41598-025-11998-5.

(5) Esmaeilnejad-Ahranjani, P.; Lotfi, M.; Zahmatkesh, A.; Esskandary, A. A. Cu-Doped Fe3O4 Nanoparticles for Efficient Detoxification of Epsilon Toxin: Toward Substituting Magnetically Recyclable Detoxifying Agent for Formaldehyde. *Toxicon* **2024**, *242*, 107707. https://doi.org/10.1016/j.toxicon.2024.107707.

(6) Amar, I. A.; Alshibani, Z. M.; AbdulQadir, M. A.; Abdalsamed, I. A.; Altohami, F. A. Oil Spill Removal from Water by Absorption on Zinc-Doped Cobalt Ferrite Magnetic Nanoparticles. *Advanced Journal of Chemistry-Section A* **2019**, *2* (4), 365–374. https://doi.org/10.33945/sami/ajca.2019.4.9.

(7) Hossein Abdolmohammad-Zadeh; Zahra Ayazi. Zinc(II)-Doped Manganese Ferrite Nanoparticles as an Efficient Magnetic Adsorbent for Cadmium Extraction from Water Samples. *Analytical and Bioanalytical Chemistry Research* **2022**, *9* (2), 209–220. https://doi.org/10.22036/abcr.2021.293274.1652.

(8) Amar, I.; Sharif, A.; Ali, M.; Alshareef, S.; Altohami, F.; Abdulqadir, M.; Ahwidi, M. M. Removal of Methylene Blue from Aqueous Solutions Using Nano-Magnetic Adsorbent Based on Zinc-Doped Cobalt Ferrite. *Chemical Methodologies* **2020**, *4* (1), 1–18. https://doi.org/10.33945/sami/chemm.2020.1.1.

(9) Li, Y.; Li, K.; Li, M.; Ge, M. Zinc-Doped Ferrite Nanoparticles as Magnetic Recyclable Catalysts for Scale-up Glycolysis of Poly(Ethylene Terephthalate) Wastes. *Advanced Powder Technology* **2022**, *33* (3), 103444. https://doi.org/10.1016/j.apt.2022.103444.

(10) Huang, X.; Xu, C.; Ma, J.; Chen, F. Ionothermal Synthesis of Cu-Doped Fe3O4 Magnetic Nanoparticles with Enhanced Peroxidase-like Activity for Organic Wastewater Treatment. *Advanced Powder Technology* **2018**, *29* (3), 796–803. https://doi.org/10.1016/j.apt.2017.12.025.

(11) Sathiyamurthy, K.; Rajeevgandhi, C.; Guganathan, L.; Bharanidharan, S.; Savithiri, S. Enhancement of Magnetic, Supercapacitor Applications and Theoretical Approach on Cobalt-Doped Zinc Ferrite Nanocomposites. *Journal of Materials Science: Materials in Electronics* **2021**, *32* (9), 11593–11606. https://doi.org/10.1007/s10854-021-05764-2.

(12) Rani, B. J.; Ravi, G.; R. Yuvakkumar; Ganesh, V.; Ravichandran, S.; M. Thambidurai; Rajalakshmi, A. P.; A. Sakunthala. Pure and Cobalt-Substituted Zinc-Ferrite Magnetic Ceramics for Supercapacitor Applications. *Applied Physics A* **2018**, *124* (7). https://doi.org/10.1007/s00339-018-1936-3.

(13) Bryan, J. D.; Gamelin, D. R. Doped Semiconductor Nanocrystals: Synthesis, Characterization, Physical Properties, and Applications. *Progress in Inorganic Chemistry* **2005**, *54*, 47–126. https://doi.org/10.1002/0471725560.ch2.

(14) Raczka, T.; Luthardt, L.; Müssig, S.; Kent, N.; Lan, Q.; Denneulin, T.; Dunin-Borkowski, R. E.; Mandel, K. Magnetically "Programming" Cobalt-Doped Iron Oxide Nanoparticles for Localized Induction Heating: Triggering a Collective Effect of Magnetic Moment Alignment on Demand. *Advanced Materials* **2025**, *37* (40). https://doi.org/10.1002/adma.202507158.

(15) Bhargava, R. N.; Gallagher, D.; Hong, X.; Nurmikko, A. Optical Properties of Manganese-Doped Nanocrystals of ZnS. *Physical Review Letters* **1994**, *72* (3), 416–419. https://doi.org/10.1103/physrevlett.72.416.

(16) Luo, D.; Wang, L.; Qiu, Y.; Huang, R.; Liu, B. Emergence of Impurity-Doped Nanocrystal Light-Emitting Diodes. *Nanomaterials* **2020**, *10* (6), 1226. https://doi.org/10.3390/nano10061226.

(17) Karan, N. S.; Sarma, D. D.; Kadam, R. M.; Pradhan, N. Doping Transition Metal (Mn or Cu) Ions in Semiconductor Nanocrystals. *The Journal of Physical Chemistry Letters* **2010**, *1* (19), 2863–2866. https://doi.org/10.1021/jz1012164.

(18) Shen, H.; Wang, H.; Li, X.; Niu, J. Z.; Wang, H.; Chen, X.; Li, L. S. Phosphine-Free Synthesis of High Quality ZnSe, ZnSe/ZnS, and Cu-, Mn-Doped ZnSe Nanocrystals. *Dalton Transactions* **2009**, No. 47, 10534. https://doi.org/10.1039/b917674h.

(19) Jana, S.; Srivastava, B. B.; Pradhan, N. Correlation of Dopant States and Host Bandgap in Dual-Doped Semiconductor Nanocrystals. *The Journal of Physical Chemistry Letters* **2011**, *2* (14), 1747–1752. https://doi.org/10.1021/jz200673q.

(20) Xie, R.; Peng, X. Synthesis of Cu-Doped InP Nanocrystals (D-Dots) with ZnSe Diffusion Barrier as Efficient and Color-Tunable NIR Emitters. *Journal of the American Chemical Society* **2009**, *131* (30), 10645–10651. https://doi.org/10.1021/ja903558r.

(21) Zhang, W.-J.; Lou, Q.; Ji, W.; Zhao, J.; Zhong, X. Color-Tunable Highly Bright Photoluminescence of Cadmium-Free Cu-Doped Zn–In–S Nanocrystals and Electroluminescence. *Chemistry of Materials* **2014**, *26* (2), 1204–1212. https://doi.org/10.1021/cm403584a.

(22) Sethi, R.; Kumar, L.; Sharma, P. K.; Pandey, A. Tunable Visible Emission of Ag-Doped CdZnS Alloy Quantum Dots. *Nanoscale Research Letters* **2009**, *5* (1). https://doi.org/10.1007/s11671-009-9449-9.

(23) Ali, F.; Das, S.; Bhandari, P.; Datta, A. Mechanism of Enhancement of Stokes Shifted Photoluminescence Quantum Yield and Lifetime from Ag(I)-Doped CdSe Nanotetrapods: Implications for Optoelectronic and Photonic Devices. *ACS Applied Nano Materials* **2023**, *6* (8), 6670–6677. https://doi.org/10.1021/acsanm.3c00385.

(24) Kroupa, D. M.; Hughes, B. K.; Miller, E. M.; Moore, D. T.; Anderson, N. C.; Chernomordik, B. D.; Nozik, A. J.; Beard, M. C. Synthesis and Spectroscopy of Silver-Doped PbSe Quantum Dots. *Journal of the American Chemical Society* **2017**, *139* (30), 10382–10394. https://doi.org/10.1021/jacs.7b04551.

(25) *Mn-doped Quantum Dots*. Cd-bioparticles.com. https://www.cd-bioparticles.com/product/mn-znse-quantum-dots-list-236.html (accessed 2026-04-30).

(26) *Manganese Doped Zinc Selenide (Mn:ZnSe) Quantum Dots (DD)*. NN-labs.com. Manganese Doped Zinc Selenide (Mn:ZnSe) Quantum Dots (DD) (accessed 2026-04-30).

(27) Weber, J. R.; Koehl, W. F.; Varley, J. B.; Janotti, A.; Buckley, B. B.; Van de Walle, C. G.; Awschalom, D. D. Quantum Computing with Defects. *PNAS* **2010**, *107* (19), 8513–8518. https://doi.org/10.1073/pnas.1003052107.

(28) Zhang, G.; Cheng, Y.; Chou, J.; Gali, Á. Material Platforms for Defect Qubits and Single-Photon Emitters. *Applied physics reviews* **2020**, *7* (3). https://doi.org/10.1063/5.0006075.

(29) Vasileios Niaouris; Durnev, M. V.; Xiayu Linpeng; Maria; Zimmermann, C.; Aswin Vishnuradhan; Yusuke Kozuka; Kawasaki, M.; Fu, K.-M. C. Ensemble Spin Relaxation of Shallow Donor Qubits in ZnO. *Physical review. B./Physical review. B* **2022**, *105* (19). https://doi.org/10.1103/physrevb.105.195202.

(30) Viitaniemi, M. L. K.; Zimmermann, C.; Niaouris, V.; D'Ambrosia, S. H.; Wang, X.; Kumar, E. S.; Mohammadbeigi, F.; Watkins, S. P.; Fu, K.-M. C. Coherent Spin Preparation of Indium Donor Qubits in Single ZnO Nanowires. *Nano Letters* **2022**, *22* (5), 2134–2139. https://doi.org/10.1021/acs.nanolett.1c04156.

(31) Xu, Y.; Schoonen, M. A. A. The Absolute Energy Positions of Conduction and Valence Bands of Selected Semiconducting Minerals. *American Mineralogist* **2000**, *85* (3-4), 543–556. https://doi.org/10.2138/am-2000-0416.

(32) Yang, Z.; Gao, M.; Wu, W.; Yang, X.; Sun, X. W.; Zhang, J.; Wang, H.-C.; Liu, R.-S.; Han, C.-Y.; Yang, H.; Li, W. Recent Advances in Quantum Dot-Based Light-Emitting Devices: Challenges and Possible Solutions. *Materials Today* **2019**, *24*, 69–93. https://doi.org/10.1016/j.mattod.2018.09.002.

(33) Wang, Q. L.; Yang, Y. F.; He, H. P.; Chen, D. D.; Ye, Z. Z.; Jin, Y. Z. One-Step Synthesis of Monodisperse In-Doped ZnO Nanocrystals. *Nanoscale Research Letters* **2010**, *5* (5), 882–888. https://doi.org/10.1007/s11671-010-9579-0.

(34) Da Silva, A.; Vancaeyzeele, C.; Vidal, F.; Dupont, L.; Aubert, P.-H. Plasmonic Al, Ga and In-Doped Zinc Oxide Nanoparticles as Key Components for the Design of Electrophoretic Inks with MWIR and LWIR Absorbance Properties. *Chemical Engineering Journal* **2024**, *497*, 154253. https://doi.org/10.1016/j.cej.2024.154253.

(35) Della Gaspera, E.; Chesman, A. S. R.; van Embden, J.; Jasieniak, J. J. Non-Injection Synthesis of Doped Zinc Oxide Plasmonic Nanocrystals. *ACS Nano* **2014**, *8* (9), 9154–9163. https://doi.org/10.1021/nn5027593.

(36) Kondev, F. G.; Wang, M.; Wang, W. J.; Naimi, S.; Audi, G. The NUBASE2020 Evaluation of Nuclear Physics Properties. *Chinese Physics C* **2021**, *45* (3). https://doi.org/10.1088/1674-1137/abddae.

(37) Canfield, D. E. Biogeochemistry of Sulfur Isotopes. *Reviews in Mineralogy and Geochemistry* **2001**, *43* (1), 607–636. https://doi.org/10.2138/gsrmg.43.1.607.

(38) Jüstel, T.; Möller, S.; Winkler, H.; Adam, W. Luminescent Materials. *Ullmann's Encyclopedia of Industrial Chemistry* **2012**. https://doi.org/10.1002/14356007.a15_519.pub2.

(39) Comptes Rendus Hebdomadaires Des Séances de l'Académie Des Sciences / Publiés... Par MM. Les Secrétaires Perpétuels. *Gallica* **1866**. oai:bnf.fr:gallica/ark:/12148/bpt6k30204.

(40) Auer, G.; Woditsch, P.; Westerhaus, A.; Jürgen Kischkewitz; Wolf-dieter Griebler; Rohe, M.; Liedekerke, M. Pigments, Inorganic, 2. White Pigments. *Ullmann's Encyclopedia of Industrial Chemistry* **2017**, 1–36. https://doi.org/10.1002/14356007.n20_n01.pub2.

(41) Wang, J.; Lim, Y.-F.; Ho, G. W. Carbon-Ensemble-Manipulated ZnS Heterostructures for Enhanced Photocatalytic H_2Evolution. *Nanoscale* **2014**, *6* (16), 9673–9673. https://doi.org/10.1039/c4nr02368d.

(42) Hao, J.; Liu, H.; Miao, J.; Lu, R.; Zhou, Z.; Zhao, B.; Xie, B.; Cheng, J.; Wang, K.; Delville, M.-H. A Facile Route to Synthesize CdSe/ZnS Thick-Shell Quantum Dots with Precisely Controlled Green Emission Properties: Towards QDs Based LED Applications. *Scientific Reports* **2019**, *9* (1). https://doi.org/10.1038/s41598-019-48469-7.

(43) Premkumar, S.; Nataraj, D.; Bharathi, G.; Ramya, S.; Thangadurai, T. D. Highly Responsive Ultraviolet Sensor Based on ZnS Quantum Dot Solid with Enhanced Photocurrent. *Scientific Reports* **2019**, *9* (1), 18704. https://doi.org/10.1038/s41598-019-55097-8.

(44) Kumar, V.; Rawal, I.; Kumar, V.; Goyal, P. K. Efficient UV Photodetectors Based on Ni-Doped ZnS Nanoparticles Prepared by Facial Chemical Reduction Method. *Physica B: Condensed Matter* **2019**, *575*, 411690. https://doi.org/10.1016/j.physb.2019.411690.

(45) Zheng, J.; Yuan, X.; Ikezawa, M.; Jing, P.; Liu, X.; Zheng, Z.; Kong, X.; Zhao, J.; Masumoto, Y. Efficient Photoluminescence of Mn^{2+} Ions in MnS/ZnS Core/Shell Quantum Dots. *The Journal of Physical Chemistry C* **2009**, *113* (39), 16969–16974. https://doi.org/10.1021/jp906390y.

(46) Srivastava, B. B.; Jana, S.; Karan, N. S.; Sayantan Paria; Jana, N. R.; Sarma, D. D.; Pradhan, N. Highly Luminescent Mn-Doped ZnS Nanocrystals: Gram-Scale Synthesis. *The Journal of Physical Chemistry Letters* **2010**, *1* (9), 1454–1458. https://doi.org/10.1021/jz100378w.

(47) Lee, G. H.; Kawazoe, T.; Ohtsu, M. Difference in Optical Bandgap between Zinc-Blende and Wurtzite ZnO Structure Formed on Sapphire (0001) Substrate. *Solid State Communications* **2002**, *124* (5-6), 163–165. https://doi.org/10.1016/s0038-1098(02)00537-9.

(48) Hamzah, N.; Samat, M. H.; Johari, N. A.; Faizal, A. F. A.; Hassan, O. H.; Ali, A. M. M.; Zakaria, R.; Hussin, N. H.; Yahya, M. Z. A.; Taib, M. F. M. FIRST-PRINCIPLE LDA+U and GGA+U CALCULATIONS on STRUCTURAL and ELECTRONIC PROPERTIES of WURTZITE ZnO. *Solid State Science and Technology* **2022**, *30* (1), 20–36.

(49) Subramani, T.; Lilova, K.; Householder, M.; Yang, S.; Lyons, J.; Navrotsky, A. Surface Energetics of Wurtzite and Sphalerite Polymorphs of Zinc Sulfide and Implications for Their Formation in Nature. *Geochimica et Cosmochimica Acta* **2023**, *340*, 99–107. https://doi.org/10.1016/j.gca.2022.11.003.

(50) Adachi, S. Properties of Group-IV, III-v and II-vi Semiconductors. **2005**. https://doi.org/10.1002/0470090340.

(51) Ghosh Chaudhuri, R.; Paria, S. Core/Shell Nanoparticles: Classes, Properties, Synthesis Mechanisms, Characterization, and Applications. *Chemical Reviews* **2011**, *112* (4), 2373–2433. https://doi.org/10.1021/cr100449n.

(52) Smagul Karazhanov; Ravindran, P.; A. Kjekshus; Helmer Fjellvåg; Svensson, B. G. Electronic Structure and Optical Properties of ZnX (X=O, S, Se, Te). *Physical Review B* **2007**, *75* (15). https://doi.org/10.1103/physrevb.75.155104.

(53) Karazhanov, S. Zh.; Ravindran, P.; Kjekshus, A.; Fjellvag, H.; Grossner, U.; Svensson, B. G. Coulomb Correlation Effects in Zinc Monochalcogenides. *Journal of Applied Physics* **2006**, *100*, 043709.

(54) Karazhanov, S. Zh.; Ravindran, P.; Kjekhus, A.; Fjellvåg, H.; Grossner, U.; Svensson, B. G. Electronic Structure and Band Parameters for ZnX (X = O, S, Se, Te). *Journal of Crystal Growth* **2006**, *287* (1), 162–168. https://doi.org/10.1016/j.jcrysgro.2005.10.061.

(55) LibreTexts. *Quantum Dots*. Engineering LibreTexts. https://eng.libretexts.org/Bookshelves/Materials_Science/Supplemental_Modules_(Materials_Science)/Semiconductors/Quantum_Dots.

(56) Senger, R. T.; Bajaj, K. K. Optical Properties of Confined Polaronic Excitons in Spherical Ionic Quantum Dots. *Physical review* **2003**, *68* (4). https://doi.org/10.1103/physrevb.68.045313.

(57) Bennett, E.; Greenberg, M. W.; Jordan, A. J.; Hamachi, L. S.; Banerjee, S.; Billinge, S. J. L.; Owen, J. S. Size Dependent Optical Properties and Structure of ZnS Nanocrystals Prepared from a Library of Thioureas. *Chemistry of Materials* **2022**, *34* (2), 706–717. https://doi.org/10.1021/acs.chemmater.1c03432.

(58) Toma, M.; Oleksandr Selyshchev; Yevhenii Havryliuk; Pop, A.; Dietrich. Optical and Structural Characteristics of Rare Earth-Doped ZnO Nanocrystals Prepared in Colloidal Solution. *Photochem* **2022**, *2* (3), 515–527. https://doi.org/10.3390/photochem2030036.

(59) Luo, W.; Liu, Y.; Chen, X. Lanthanide-Doped Semiconductor Nanocrystals: Electronic Structures and Optical Properties. *Science China Materials* **2015**, *58* (10), 819–850. https://doi.org/10.1007/s40843-015-0091-9.

(60) Schwartz, D. A.; Norberg, N. S.; Nguyen, Q. P.; Parker, J. M.; Gamelin, D. R. Magnetic Quantum Dots: Synthesis, Spectroscopy, and Magnetism of Co2+- and Ni2+-Doped ZnO Nanocrystals. *Journal of the American Chemical Society* **2003**, *125* (43), 13205–13218. https://doi.org/10.1021/ja036811v.

(61) Norberg, N. S.; Gamelin, D. R. Influence of Surface Modification on the Luminescence of Colloidal ZnO Nanocrystals. *The Journal of Physical Chemistry B* **2005**, *109* (44), 20810–20816. https://doi.org/10.1021/jp0535285.

(62) Zhang, W.; Li, Y.; Zhang, H.; Zhou, X.; Zhong, X. Facile Synthesis of Highly Luminescent Mn-Doped ZnS Nanocrystals. *Inorganic Chemistry* **2011**, *50* (20), 10432–10438. https://doi.org/10.1021/ic201547g.

(63) Yim, K.; Lee, J.; Lee, D.; Lee, M.; Cho, E.; Lee, H. S.; Nahm, H.-H.; Han, S. Property Database for Single-Element Doping in ZnO Obtained by Automated First-Principles Calculations. *Scientific Reports* **2017**, *7* (1). https://doi.org/10.1038/srep40907.

(64) *Aluminum doped zinc oxide nanoparticle ink*. Sigmaaldrich.com. https://www.sigmaaldrich.com/US/en/product/aldrich/921564?utm_source=google&utm_medium=cpc&utm_campaign=20790375250&utm_content=154400301983&gad_source=1&gad_campaignid=20790375250&gbraid=0AAAAAD8kLQRdzxoPoilrsHAC2UpOpyAI8&gclid=Cj0KCQjw4a3OBhCHARIsAChaq (accessed 2026-04-30).

(65) *Zinc Sulphide Phosphorescence*. PhysicsOpenLab. https://physicsopenlab.org/2019/02/06/zinc-sulphide-phosphorescence/.

(66) Janotti, A.; Van de Walle, C. G. Fundamentals of Zinc Oxide as a Semiconductor. *Reports on Progress in Physics* **2009**, *72* (12), 126501. https://doi.org/10.1088/0034-4885/72/12/126501.

(67) Faucheaux, J. A.; Stanton, A. L. D.; Jain, P. K. Plasmon Resonances of Semiconductor Nanocrystals: Physical Principles and New Opportunities. *The Journal of Physical Chemistry Letters* **2014**, *5* (6), 976–985. https://doi.org/10.1021/jz500037k.

(68) Pradhan, N.; Sarma, D. D. Advances in Light-Emitting Doped Semiconductor Nanocrystals. *The Journal of Physical Chemistry Letters* **2011**, *2* (21), 2818–2826. https://doi.org/10.1021/jz201132s.

(69) Cargnello, M.; Johnston-Peck, A. C.; Diroll, B. T.; Wong, E.; Datta, B.; Damodhar, D.; Doan-Nguyen, V. V. T.; Herzing, A. A.; Kagan, C. R.; Murray, C. B. Substitutional Doping in Nanocrystal Superlattices. *Nature* **2015**, *524* (7566), 450–453. https://doi.org/10.1038/nature14872.

(70) Erwin, S. C.; Zu, L.; Haftel, M. I.; Efros, A. L.; Kennedy, T. P.; Norris, D. G. Doping Semiconductor Nanocrystals. *Nature* **2005**, *436* (7047), 91–94. https://doi.org/10.1038/nature03832.

(71) Look, D. C.; Sizelove, J. R. Dislocation Scattering in GaN. *Physical Review Letters* **1999**, *82* (6), 1237–1240. https://doi.org/10.1103/physrevlett.82.1237.

(72) Gamelin, D. R.; Gudel, H. U. Upconversion Processes in Transition Metal and Rare Earth Metal Systems. In *Transition Metal and Rare Earth Compounds*; Springer: Berlin, Heidelberg, 2014; pp. 1–56.

(73) Norberg, N. S.; Kittilstved, K. R.; Amonette, J. E.; Kukkadapu, R. K.; Schwartz, D. S.; Gamelin, D. R. Synthesis of Colloidal Mn2+:ZnO Quantum Dots and High-TC Ferromagnetic Nanocrystalline Thin Films. *Journal of the American Chemical Society* **2004**, *126* (30), 9387–9398. https://doi.org/10.1021/ja048427j.

(74) Ghica, D.; Vlaicu, I. D.; Stefan, M.; Maraloiu, V. A.; Joita, A. C.; Ghica, C. Tailoring the Dopant Distribution in ZnO:Mn Nanocrystals. *Scientific Reports* **2019**, *9* (1). https://doi.org/10.1038/s41598-019-43388-z.

(75) Dalpian, G. M.; Chelikowsky, J. R. Self-Purification in Semiconductor Nanocrystals. *Physical Review Letters* **2006**, *96* (22). https://doi.org/10.1103/physrevlett.96.226802.

(76) G. Counio; S. Esnouf; Gacoin, and T.; J.-P. Boilot. CdS:Mn Nanocrystals in Transparent Xerogel Matrices: Synthesis and Luminescence Properties. *Journal of physical chemistry* **1996**, *100* (51), 20021–20026. https://doi.org/10.1021/jp961937i.

(77) Stefan, M.; Nistor, S. V.; Ghica, D.; Mateescu, C. D.; Nikl, M.; Kucerkova, R. Substitutional and Surface Mn2+ Centers in Cubic ZnS:Mn Nanocrystals. A Correlated EPR and Photoluminescence Study. *Physical Review B* **2011**, *83* (4). https://doi.org/10.1103/physrevb.83.045301.

(78) Sooklal, K.; Cullum, B. S.; Angel, M.; Murphy, C. J. Photophysical Properties of ZnS Nanoclusters with Spatially Localized Mn^{2+}. *The Journal of Physical Chemistry* **1996**, *100* (11), 4551–4555. https://doi.org/10.1021/jp952377a.

(79) Bhargava, R. N. Doped Nanocrystalline Materials — Physics and Applications. *Journal of Luminescence* **1996**, *70* (1-6), 85–94. https://doi.org/10.1016/0022-2313(96)00046-4.

(80) Murray, C. B.; Norris, D. J.; Bawendi, M. G. Synthesis and Characterization of Nearly Monodisperse CdE (E = Sulfur, Selenium, Tellurium) Semiconductor Nanocrystallites. *Journal of the American Chemical Society* **1993**, *115* (19), 8706–8715. https://doi.org/10.1021/ja00072a025.

(81) Peng, X.; Manna, L.; Yang, W.; Wickham, J.; Scher, E.; Kadavanich, A.; Alivisatos, A. P. Shape Control of CdSe Nanocrystals. *Nature* **2000**, *404* (6773), 59–61. https://doi.org/10.1038/35003535.

(82) Xueyuan, C.; Wenqin, L.; Yongsheng, L.; Guokui, L. Recent Progress on Spectroscopy of Lanthanide Ions Incorporated in Semiconductor Nanocrystals. *Journal of Rare Earths* **2007**, *25* (5), 515–525. https://doi.org/10.1016/s1002-0721(07)60555-9.

(83) Bol, A. A.; van Beek, R.; Meijerink, A. On the Incorporation of Trivalent Rare Earth Ions in II−vi Semiconductor Nanocrystals. *Chemistry of Materials* **2002**, *14* (3), 1121–1126. https://doi.org/10.1021/cm011195s.

(84) Gerbreders, V.; Krasovska, M.; Sledevskis, E.; Gerbreders, A.; Mihailova, I.; Tamanis, E.; Ogurcovs, A. Hydrothermal Synthesis of ZnO Nanostructures with Controllable Morphology Change. *CrystEngComm* **2020**, *22* (8), 1346–1358. https://doi.org/10.1039/C9CE01556F.

(85) Baruah, S.; Dutta, J. Hydrothermal Growth of ZnO Nanostructures. *Science and Technology of Advanced Materials* **2009**, *10* (1), 013001. https://doi.org/10.1088/1468-6996/10/1/013001.

(86) Peng, X. An Essay on Synthetic Chemistry of Colloidal Nanocrystals. *Nano Research* **2009**, *2* (6), 425–447. https://doi.org/10.1007/s12274-009-9047-2.

(87) Vlaskin, V. A.; Barrows, C. J.; Erickson, C. S.; Gamelin, D. R. Nanocrystal Diffusion Doping. *Journal of the American Chemical Society* **2013**, *135* (38), 14380–14389. https://doi.org/10.1021/ja4072207.

(88) Janotti, A.; Van de Walle, C. G. Oxygen Vacancies in ZnO. *Applied Physics Letters* **2005**, *87*, 122102.

(89) Reiss, P.; Protière, M.; Li, L. Core/Shell Semiconductor Nanocrystals. *Small* **2009**, *5* (2), 154–168. https://doi.org/10.1002/smll.200800841.

(90) Quan, Z.; Wang, Z.; Yang, P.; Lin, J.; Fang, J. Synthesis and Characterization of High-Quality ZnS, ZnS:Mn2+, and ZnS:Mn2+/ZnS (Core/Shell) Luminescent Nanocrystals. *Inorganic Chemistry* **2007**, *46* (4), 1354–1360. https://doi.org/10.1021/ic061917n.

(91) Aboulaich, A.; Geszke, M.; Balan, L.; Ghanbaja, J.; Medjahdi, G.; SchneiderR. Water-Based Route to Colloidal Mn-Doped ZnSe and Core/Shell ZnSe/ZnS Quantum Dots. *Inorganic Chemistry* **2010**, *49* (23), 10940–10948. https://doi.org/10.1021/ic101302q.

(92) David Bernard Williams; Carter, B. C. *Transmission Electron Microscopy. 3, Imaging*; Springer: New York, 2009.

(93) Bünzli, J.-C. G.; Piguet, C. Taking Advantage of Luminescent Lanthanide Ions. *Chemical Society Reviews* **2005**, *34* (12), 1048. https://doi.org/10.1039/b406082m.

(94) Mayer, U.; Gutmann, V.; Gerger, W. The Acceptor Number - a Quantitative Empirical Parameter for the Electrophilic Properties of Solvents. *Monatshefte f□r Chemie* **1975**, *106* (6), 1235–1257. https://doi.org/10.1007/bf00913599.

(95) D'Amico, P.; Calzolari, A.; Ruini, A.; Catellani, A. New Energy with ZnS: Novel Applications for a Standard Transparent Compound. *Scientific Reports* **2017**, *7* (1), 16805. https://doi.org/10.1038/s41598-017-17156-w.

(96) Tian, Y.; Zhao, Y.; Tang, H.; Zhou, W.; Wang, L.; Zhang, J. Synthesis of ZnS Ultrathin Nanowires and Photoluminescence with Mn2+ Doping. *Materials Letters* **2015**, *148*, 151–154. https://doi.org/10.1016/j.matlet.2015.02.065.

(97) Li, Z.; Liu, B.; Li, X.; Yu, S.; Wang, L.; Hou, Y.; Zou, Y.; Yao, M.; Li, Q.; Zou, B.; Cui, T.; Zou, G.; Wang, G.; Liu, Y. Synthesis of ZnS Nanocrystals with Controllable Structure and Morphology and Their Photoluminescence Property. *Nanotechnology* **2007**, *18* (25), 255602. https://doi.org/10.1088/0957-4484/18/25/255602.

(98) Wang, X.; Shi, J.; Feng, Z.; Li, M.; Li, C. Visible Emission Characteristics from Different Defects of ZnS Nanocrystals. *Physical Chemistry Chemical Physics* **2011**, *13* (10), 4715. https://doi.org/10.1039/c0cp01620a.

(99) Zhao, Q.; Hou, L.; Huang, R. Synthesis of ZnS Nanorods by a Surfactant-Assisted Soft Chemistry Method. *Inorganic Chemistry Communications* **2003**, *6* (7), 971–973. https://doi.org/10.1016/s1387-7003(03)00146-1.

(100) Chen, X.; Xu, H.; Xu, N.; Zhao, F.; Lin, W.; Lin, G.; Fu, Y.-L.; Huang, Z.-L.; Wang, H.-Z.; Wu, M. Kinetically Controlled Synthesis of Wurtzite ZnS Nanorods through Mild Thermolysis of a Covalent Organic−Inorganic Network. *Inorganic Chemistry* **2003**, *42* (9), 3100–3106. https://doi.org/10.1021/ic025848y.

(101) Djurišić, Aleksandra B.; Leung, Y. H. Optical Properties of ZnO Nanostructures. *Small* **2006**, *2* (8-9), 944–961. https://doi.org/10.1002/smll.200600134.

(102) Chen, O.; Zhao, J.; Chauhan, V. P.; Cui, J.; Wong, C.; Harris, D. K.; Wei, H.; Han, H.-S.; Fukumura, D.; Jain, R. K.; Bawendi, M. G. Compact High-Quality CdSe–CdS Core–Shell Nanocrystals with Narrow Emission Linewidths and Suppressed Blinking. *Nature Materials* **2013**, *12* (5), 445–451. https://doi.org/10.1038/nmat3539.

(103) Xi, G.; Wang, C.; Wang, X.; Zhang, Q.; Xiao, H. From ZnS·en0.5 Nanosheets to Wurtzite ZnS Nanorods under Solvothermal Conditions. *The Journal of Physical Chemistry C* **2008**, *112* (6), 1946–1952. https://doi.org/10.1021/jp709807t.

(104) Kim, Y.; Kim, J.-Y.; Jang, D.-J. One-Pot and Template-Free Fabrication of ZnS·(Ethylenediamine)$_{0.5}$ Hybrid Nanobelts. *The Journal of Physical Chemistry C* **2012**, *116* (18), 10296–10302. https://doi.org/10.1021/jp212420x.

(105) Huang, X.; Li, J.; Zhang, Y.; Mascarenhas, A. From 1D Chain to 3D Network: Tuning Hybrid II-vi Nanostructures and Their Optical Properties. *Journal of the American Chemical Society* **2003**, *125* (23), 7049–7055. https://doi.org/10.1021/ja0343611.

(106) Yu, S.-H. .; Yoshimura, M. Shape and Phase Control of ZnS Nanocrystals: Template Fabrication of Wurtzite ZnS Single-Crystal Nanosheets and ZnO Flake-like Dendrites from a Lamellar Molecular Precursor ZnS·(NH2CH2CH2NH2)0.5. *Advanced Materials* **2002**, *14* (4), 296–300. https://doi.org/10.1002/1521-4095(20020219)14:4%3C296::aid-adma296%3E3.0.co;2-6.